

MODELING AND ANALYSIS OF DIAGNOSTIC

FRACTURE INJECTION

TESTS (DFITs)

by

Recep Bakar

A thesis submitted to the Faculty and the Board of Trustees of the Colorado School of Mines in partial fulfillment of the requirements for the degree of Master of Science (Petroleum Engineering).

Golden, Colorado

Date: _____

Signed:

Recep Bakar

Signed:

Dr. Erdal Ozkan
Thesis Advisor

Golden, Colorado

Date: _____

Signed:

Dr. Erdal Ozkan
Professor and Head
Department of Petroleum Engineering

ABSTRACT

Diagnostic fracture injection tests (DFIT) are used as an indirect method to determine closure pressure and formation effective permeability in unconventional reservoirs as a first step in formation evaluation. The information obtained from DFIT is particularly useful because it is obtained before any production for a given well is available.

In DFIT, a small fracture is created by injecting few barrels of completion fluid until formation breaks down and a fracture is initiated and propagates a short distance into the reservoir. Then, injection is stopped and the pressure decline (or falloff) is monitored. From this pressure decline, the effective permeability of the formation is estimated by Nolte's G-function, log-log plot, or square root of time analysis.

In this research, the viability of the common DFIT analysis techniques was investigated for unconventional reservoirs with and without micro-fractures by using a numerical hydraulic fracturing simulator, CFRAC. The results of numerical simulations were investigated to assess the impact of permeability, residual fracture aperture, and complex fracture networks on conventional DFIT interpretations.

For the example considered in this work, the commonly used G-function analysis yielded estimates of permeability over an order of magnitude higher than the simulated matrix permeability. Error in the G-function estimates of permeability were higher for higher matrix permeability and in the existence of a fracture network. On the other hand, straight-line analysis of Δp versus G-time yielded much closer (in the same order of magnitude) estimates of permeability.

TABLE OF CONTENTS

| | |
|---|------|
| ABSTRACT | iii |
| LIST OF FIGURES | vii |
| LIST OF TABLES | ix |
| LIST OF SYMBOLS | x |
| ACKNOWLEDGEMENTS | xiii |
| DEDICATION | xiv |
| CHAPTER 1 INTRODUCTION | 1 |
| 1.1 Introduction..... | 1 |
| 1.2 Problem statement..... | 2 |
| 1.3 Objective of the Study | 3 |
| CHAPTER 2 BACKGROUND AND LITERATURE REVIEW | 4 |
| 2.1 Acquisition Procedure for DFIT..... | 4 |
| 2.2 Diagnostic Plots for DFIT..... | 6 |
| 2.2.1 G-function Analysis | 6 |
| 2.2.2 Sqrt(t) Analysis | 8 |
| 2.2.3 Log-Log Pressure Derivative..... | 9 |
| 2.2.4 After Closure Analysis (ACA)..... | 10 |
| 2.3 Typical Mistakes Encountered in DFIT Analysis | 12 |

| | | |
|--|---|----|
| 2.3.1 | Incorrect Instantaneous Shut-in Pressure (ISIP) Determination | 12 |
| 2.3.2 | Selection of Closure Point | 13 |
| 2.3.3 | Effect of Injection Time and Pump Rate | 14 |
| 2.3.4 | Phase Segregation and Gas Entry | 15 |
| 2.3.5 | Loss of Hydrostatic Head..... | 15 |
| 2.3.6 | Design of Test Duration..... | 16 |
| CHAPTER 3 MATHEMATICAL MODELING..... | | 21 |
| 3.1 | CFRAC Model | 21 |
| 3.1.1 | Mechanical calculations..... | 23 |
| 3.1.2 | Fracture initiation and propagation | 23 |
| 3.2 | Simulation description | 24 |
| 3.3 | Fracture geometries | 24 |
| 3.4 | Details of simulation parameters | 26 |
| CHAPTER 4 RESULTS AND DISCUSSIONS..... | | 28 |
| 4.1 | Simulation results | 28 |
| 4.1.1 | Case 1..... | 28 |
| 4.1.2 | Case 2..... | 32 |
| 4.1.3 | Case 3..... | 35 |
| 4.1.4 | Case 4..... | 39 |
| 4.2 | Discussions | 43 |

CHAPTER 5 CONCLUSIONS AND RECOMMENDATIONS45

REFERENCES47

LIST OF FIGURES

| | | |
|-------------|--|----|
| Figure 2.1 | A common DFIT Procedure. Rate and surface pressure are marked by black and red, respectively | 5 |
| Figure 2.2 | A common G-Function Plot | 7 |
| Figure 2.3 | An example of Sqrt(t) Plot..... | 9 |
| Figure 2.4 | An example of Log-Log Plot..... | 10 |
| Figure 2.5 | After Closure Analysis (ACA) Log Plot | 11 |
| Figure 2.6 | Extrapolation of the pressure versus log of time to find actual ISIP | 13 |
| Figure 2.7 | G-function Plot with the correct and incorrect Closure Points..... | 14 |
| Figure 2.8 | An example of gas-entry during the fall-off period for an actual treatment data .. | 16 |
| Figure 2.9 | An example of the estimated time for the fracture closure depending on both pumping time and system permeability | 18 |
| Figure 2.10 | The log-log plot of pressure change versus shut-in time..... | 19 |
| Figure 2.11 | An example of the created complex fracture network..... | 20 |
| Figure 3.1 | Hydraulic fracture geometry and dimension used for Cases 1, 2 and 3. | 25 |
| Figure 3.2 | Discrete fracture network (DFN) and Hydraulic fracture (red) used for Case 4 ... | 26 |
| Figure 4.1 | The G-function curve for Case 1 | 29 |
| Figure 4.2 | The plot of Δp versus G for Case 1 | 30 |
| Figure 4.3 | The log-log plot of Δp versus G for Case 1 | 30 |
| Figure 4.4 | The plot of Δp versus G within the linear flow interval for Case 1..... | 31 |
| Figure 4.5 | The G-function curve for Case 2 | 32 |

| | | |
|-------------|---|----|
| Figure 4.6 | The plot of Δp versus G for Case 2 | 33 |
| Figure 4.7 | The log-log plot of Δp versus G for Case 2 | 34 |
| Figure 4.8 | The plot of Δp versus G within the linear flow interval for Case 2..... | 34 |
| Figure 4.9 | The G-function curve for Case 3 | 36 |
| Figure 4.10 | The plot of Δp versus G for Case 3 | 37 |
| Figure 4.11 | The log-log plot of Δp versus G for Case 3 | 37 |
| Figure 4.12 | The plot of Δp versus G within the linear flow interval for Case 3..... | 38 |
| Figure 4.13 | The G-function curve for Case 4 | 40 |
| Figure 4.14 | The plot of Δp versus G for Case 4 | 41 |
| Figure 4.15 | The log-log plot of Δp versus G for Case 4..... | 41 |
| Figure 4.16 | The plot of Δp versus G within the linear flow interval for Case 4..... | 42 |

LIST OF TABLES

| | |
|---|----|
| Table 3.1 Fundamental simulation parameters for four cases investigated | 24 |
|---|----|

LIST OF SYMBOLS

| | |
|---|--------------------|
| Half length of the crack..... | a |
| Pore compressibility..... | $(c)_m$ |
| Fracture compressibility..... | $(c)_f$ |
| Fracture compliance..... | c_f |
| Leakoff coefficient..... | C_L |
| Total compressibility | c_t |
| Total compressibility of the matrix..... | $(c_t)_m$ |
| Total compressibility of the fracture..... | $(c_t)_f$ |
| Hydraulic aperture | e |
| Young`s modulus | E |
| Void aperture when the net pressure is equal to zero | E_0 |
| Open aperture of each element | E_{open} |
| Linear flow regime function | F_L |
| Shear Modulus | G |
| G-time | $G, G(\Delta t_D)$ |
| G-time at closure..... | G_c |
| Permeability of the leakoff system related to the fracture face | k |
| Matrix permeability | k_m |

| | |
|---|---------------------------|
| Fracture permeability | k_f |
| Stress intensity factor | K_I |
| Pore pressure | p |
| Closure pressure | p_c |
| Instantaneous Shut-In Pressure | p_{ISIP} |
| Bottom-hole well pressure | P_w |
| Differential pressure between bottom-hole shut-in pressure at the end of pumping time and bottom-hole pressure | $\Delta p, \Delta P_{wf}$ |
| Flux rate | q_{flux} |
| Leakoff rate | $q_{leakoff}$ |
| Storage ratio | r_p |
| Source term for a well | S |
| Fracture transmissivity | T |
| Time | t |
| The time to reach the fracture closure | t_c |
| Pumping time | t_p |
| Time to reach the pseudoradial flow | t_{pr} |
| Dimensionless time | $\Delta t_D, t_{Dxf}$ |
| Fracture width | w |

| | |
|--|-------------------|
| Fracture half-length..... | x_f |
| Unit conversion constant..... | β |
| Void aperture | ε |
| Density | ρ |
| Viscosity | μ |
| Poisson`s ratio..... | ν |
| Matrix porosity..... | ϕ, ϕ_m |
| Fracture porosity | ϕ_f |
| Effective normal stress..... | σ_n' |
| Pressure when the void aperture closes to 90% of E_0 | $\sigma_{n,Eref}$ |
| Change in the normal stress due to back stress created by the deformation..... | $\Delta\sigma_n$ |

ACKNOWLEDGEMENTS

First and foremost, praise and glory be to Allah, the most gracious, the most merciful, for enabling me to successfully complete this study.

I would like to express my sincere appreciation to my advisor, Dr. Erdal Ozkan, who encouraged and helped me during my master's program at Colorado School of Mines. I also would like to express my warm appreciation to my committee members, Dr. Hossein Kazemi and Dr. Azra Nur Tutuncu, for their great support, help, patience and kindness during my study. I especially thank Dr. Jennifer Miskimins for her help and guidance. I also extend my thanks to all faculty and staff in the Petroleum Engineering Department at Colorado School of Mines. This research project was supported by the Unconventional Reservoir Engineering Consortium (UREP) at Colorado School of Mines. I would like to thank the members of the UREP consortium for making this project possible.

Special thanks go to Dr. Mark McClure for giving us permission to use CFRAC for this study.

I also would like to thank my friend, Ilham Permata for his help and support in this research and acknowledge the support of my friends at Colorado School of Mines.

Most importantly, I would like to express my special thanks to my wife, who has endured a lot of difficulties with me. Mom, Dad, Sister and other family members, thanks for your support, guidance and help. I love you all.

DEDICATION

To Esra Bakar, my lovely wife, my family, my friends

CHAPTER 1

INTRODUCTION

1.1 Introduction

Over the last 15 years, production from the unconventional reservoirs in the US has been growing due, mostly, to the success of hydraulic fracturing (Barree et al. 2015). In hydraulic fracturing, a fluid, usually including some proppants and chemicals, is injected into the low-permeability formation at high pressure to create fracture networks. The injection pressure must exceed the minimum horizontal stress in the rock to initiate and form a fracture network. The resulting production from the reservoir is a combined function of the effectiveness of the fracture network and the prevailing formation permeability. Therefore, for the assessment of the production potential of an unconventional formation, it is important to know the matrix permeability and minimum horizontal stress.

Although matrix permeabilities are obtained from pressure-transient tests in conventional reservoirs, this approach is not viable in unconventional reservoirs prior to fracturing because there is not enough production unless the formation is fracture stimulated. Diagnostic fracture injection tests (DFIT), which are also called mini-frac tests, have been used as an alternative in these cases to estimate both the minimum horizontal stress and matrix permeability. During DFIT, a mini-frac is created by injecting a high-pressure fluid. Then, injection is stopped and pressure decay is monitored to estimate the minimum horizontal stress or closure pressure and the matrix permeability. DFITs have also been used to estimate other reservoir properties, such as pore pressure and hydraulic fracture treatment parameters.

1.2 Problem Statement

To estimate the closure pressure and formation effective permeability from a DFIT, several methods have been proposed. These methods are the square root of time analysis, log-log plot, and the G-function plot. However, these methods for DFIT analysis are based on several assumptions that do not necessarily apply to unconventional reservoirs. Some of these assumptions are the following (Nolte 1979, 1986, and 1988):

- Constant fracture height with symmetric bi-wing geometry
- Continuous, stable propagation of fluid while performing the DFIT
- Immediate stop of fracture growth when pumping is stopped
- Elastic continuum
- Constant pressure injection of a power-law fluid
- Unobstructed and complete closure of the fracture

Also inherent in these assumptions is the perception of the reservoir as a homogenous porous medium. These assumptions are likely to hold in most conventional and tight-gas reservoirs, for which the DFIT analysis was originally developed. However, unconventional reservoirs are petrophysically complex and their heterogeneity is further exacerbated by the existence of a fracture network. Under these conditions, symmetric, bi-wing fractures are not a common occurrence and fracture extension can continue after pumping is stopped. Moreover, fractures do not completely close due to fracture surface roughness. Therefore, uncontested acceptance and application of DFIT analysis is not warranted for unconventional reservoirs; yet the consequences of violating the standard assumptions and the potential magnitude of errors in the estimations various parameters from DFIT analysis of unconventional formations have not been documented in the literature.

1.3 Objective of the Study

The main objective of this research is to assess the ranges of applicability of DFIT analysis in unconventional reservoirs, provide a sense of the magnitude of error in the estimation of fracture and reservoir properties, and make suggestions to improve the analysis of DFIT data based on the examples generated by the CFRAC (Complex Fracturing ReseArch Code) simulator.

The specific objectives of this study can be listed as:

- To understand the consequences of conventional assumptions in the application of DFIT to unconventional formations
- To investigate the sensitivity of DFIT analysis to matrix permeability, residual fracture aperture, and presence of natural fractures
- To recommend guidelines for better estimation of formation permeability

CHAPTER 2

BACKGROUND AND LITERATURE REVIEW

2.1 Acquisition Procedure for DFIT

To begin with, the wellbore is filled with the fracturing fluid at a low to moderate rate until a positive surface pressure is obtained during a common DFIT. As shown in Figure 2.1 (Barree et al. 2015), pressure increases until the initial breakdown is observed. When a new fracture is created, pressure displays a rapid decrease whereas it exhibits a plateau in the event of dilation of existing fractures within the formation. When the breakdown is observed, the injection rate is ramped up to the maximum rate for the existing horsepower. The maximum rate is kept constant for 3 to 5 minutes (marked as Stage 2 in Figure 2.1). This is usually followed by a step-down rate (Stage 3 in Figure 2.1) to estimate pressure losses due to perforations and tortuosity. Next, the rate is instantly lowered to zero and the instantaneous shut-in pressure (ISIP) (Stage 4 in Figure 2.1) is estimated. Finally, the falloff pressure is monitored for as long as possible or needed in order to estimate the reservoir permeability.

Matrix permeability can be estimated from the fall-off period of a DFIT test by using the following equations (Nolte 1979; Nolte 1986; Economides and Nolte 1987; Nolte 1988).

$$\Delta p = \frac{\pi C_L \sqrt{t_p}}{2c_f} G(\Delta t_D) \quad (2.1)$$

where

$$\Delta p = P_w(\Delta t_D = 0) - P_w(\Delta t_D) \quad (2.2)$$

$$C_L = 0.00118(p_c - p) \sqrt{\frac{k_m \phi c_t}{\mu}}; [C_L \text{ in ft}/\sqrt{\text{min}}] \quad (2.3)$$

$$c_f = \left[\frac{\pi(1-\nu^2)}{2E} \right] x_f \quad (2.4)$$

$$G(\Delta t_D) = \left\{ \frac{16}{3\pi} \left[(1 + \Delta t_D)^{\frac{3}{2}} - (\Delta t_D)^{\frac{3}{2}} - 1 \right] \right\} \quad (2.5)$$

$$\Delta t_D = \frac{t - t_p}{t_p} \quad (2.6)$$

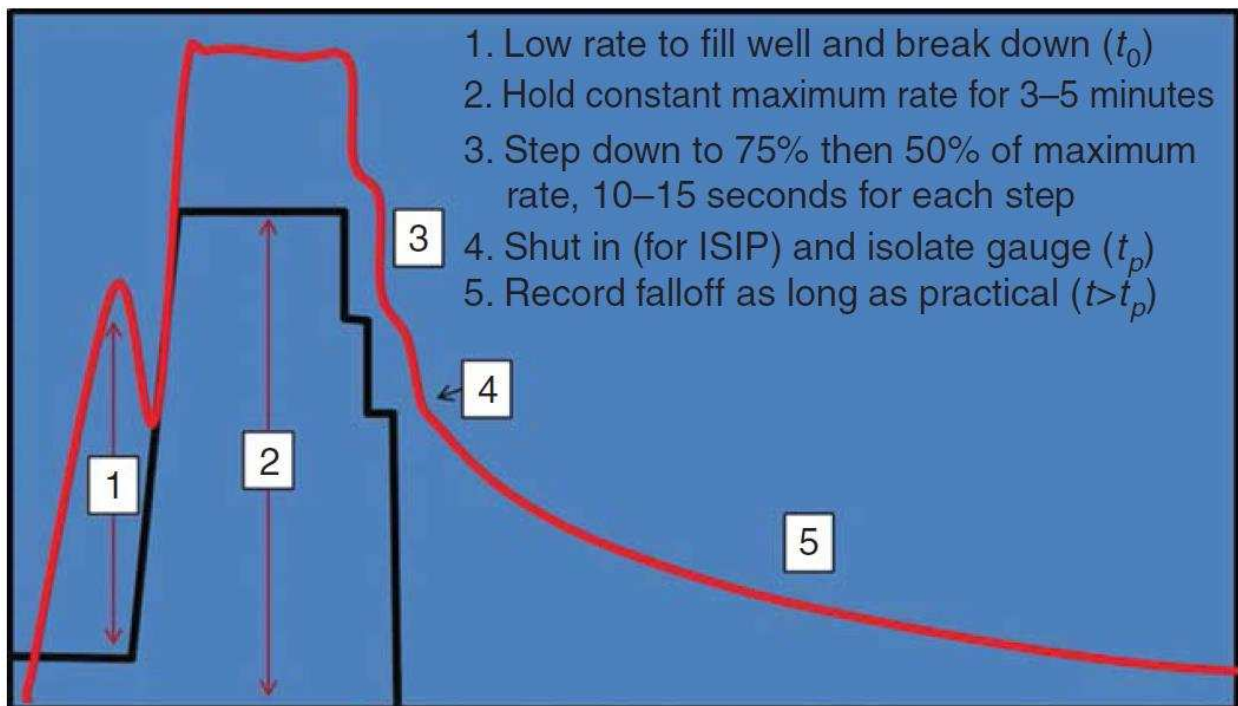


Figure 2.1 A common DFIT Procedure. Rate and surface pressure are marked by black and red, respectively (Barree et al. 2015).

In Equation 2.6, t is total time and t_p is total pumping time. Rewriting the Equation 2.1, we have

$$\Delta p = mG(\Delta t_D) \quad (2.7)$$

where

$$m = \frac{\pi C_L \sqrt{t_p}}{2c_f} \quad (2.8)$$

Equation 2.7 suggests that a plot of Δp vs $G(\Delta p)$ should yield a straight line with slope given by Equation 2.8. Knowing the slope, m , C_L can be calculated from Equation 2.8, and the matrix permeability is calculated from Equation 2.9 (Eker et al. 2015).

$$k_m = \frac{\mu C_L^2}{\phi c_t (0.00118(p_c - p))^2} \quad (2.9)$$

2.2 Diagnostic Plots for DFIT

The diagnostic plots for pre-closure DFIT analysis can be classified as the G-function, square-root of shut-in time, and $\log(\Delta P_{wf})$ - $\log(\Delta t)$ plots and their appropriate pressure derivatives. After closure analysis is also an important part of the DFIT analysis. Each of these techniques is explained for both pre-closure and after closure analysis in the following sections.

2.2.1 G-function Analysis

The G-function, which was introduced by Nolte (1979, 1986, and 1988), is a dimensionless function that is commonly used in the analysis of DFIT data. In this method, pressure, derivative (dP/dG) and semi-log derivative ($G \cdot dP/dG$) of pressure with respect to the G-function are plotted versus G-time. In this approach, the G-function represents the elapsed time after shut-in normalized to the duration of fracture extension.

The G-function analysis requires drawing a straight line that is tangent to the semi-log derivative of the pressure versus G-function curve and passes through the origin. The G-function time for the fracture closure corresponds to the deviation of the semi-log derivative from the straight line and the fracture closure pressure can be read from the pressure curve at that time.

Figure 2.2 shows an example of the G-function plot, which has the pressure and appropriate derivatives of pressure, and depicts the estimation of fracture closure time and pressure.

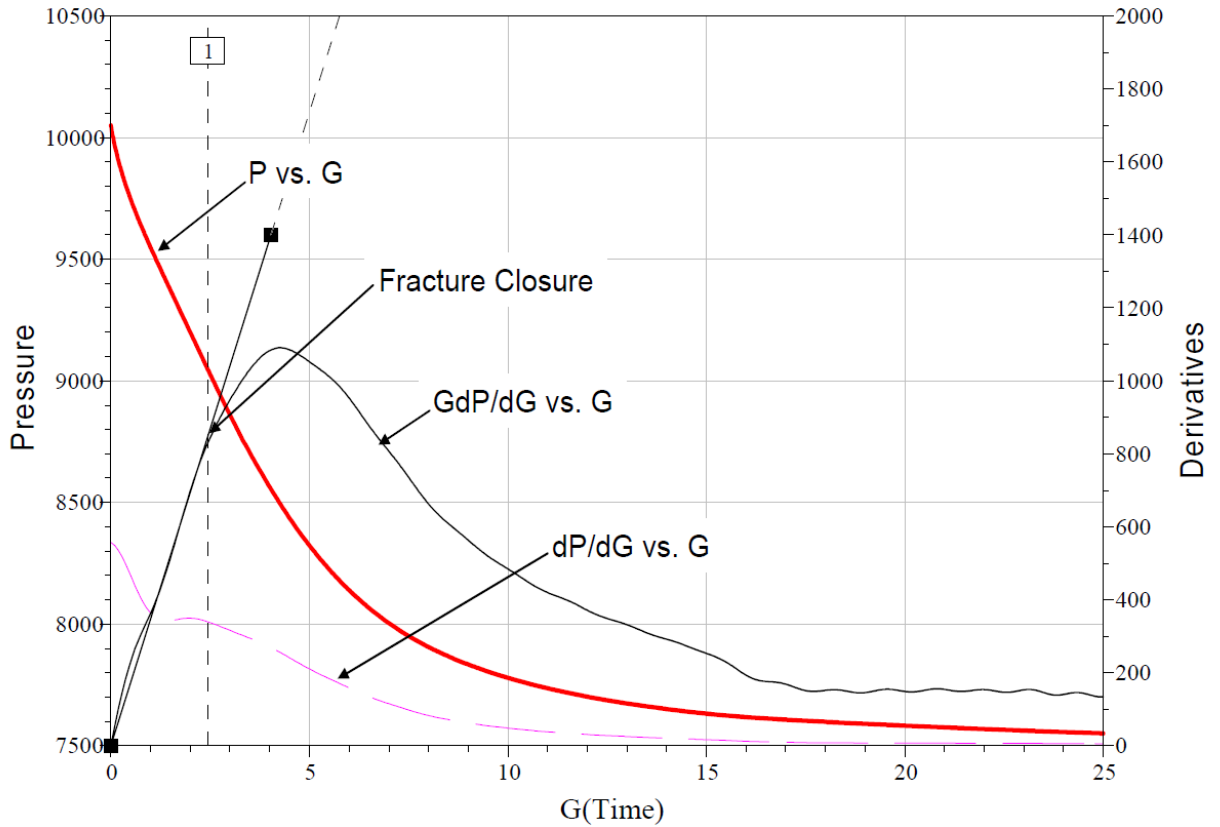


Figure 2.2 A common G-Function Plot (Barree et al. 2007).

The non-ideal (non-linear) behaviors in the G-function plot are thought to be results of various factors not considered in the original G-function model, such as fracture height recession or transverse fracture storage (concave upward), pressure dependent leakoff (concave down), and fracture tip extension, where the fracture propagates after the well shut-in. Therefore, Barree et al. (2007) recommended not to pick closure time and pressure until $(G \cdot dP/dG)$ curve stops increasing in total G-time.

The matrix permeability may be directly estimated from G-function analysis using the following equation (Barree et al. 2007):

$$k_m = 0.0086\mu \frac{\sqrt{0.01*(p_{ISIP}-p_c)}}{\phi_{c_t} \left(\frac{G_c E r_p}{0.038} \right)^{1.96}} \quad (2.10)$$

where k_m is estimated matrix permeability, p_{ISIP} is Instantaneous Shut-In Pressure (ISIP), p_c is closure pressure, ϕ is porosity, c_t is total compressibility, G_c is G-time at closure, E is Young's modulus, r_p is storage ratio and μ is fluid viscosity.

2.2.2 Square-root of Time Analysis

Square-root of time, \sqrt{t} , plot is also used to analyze DFIT data along with other methods. Figure 2.3 shows an example of a Sqrt(t) plot where pressure, its derivative ($dP/d\sqrt{t}$), and semi-log derivative ($\sqrt{t} * dP/d\sqrt{t}$) with respect to square root of time are plotted. Similar to the G-function analysis, a straight line that passes through the origin and is tangent to the semi-log derivative of the pressure versus Sqrt(t) curve must be drawn for the Sqrt(t) analysis. Then, the maximum point of the amplitude of the derivative (the inflection point) should be picked as fracture closure time. Having chosen the fracture closure time, the corresponding closure pressure can be read from the pressure versus Sqrt(t) curve. [Note that the sqrt(t) plot is often incorrectly analyzed to determine the fracture closure time and pressure. It must be emphasized that the closure time is not the deviation point from the straight line; instead it is the inflection point.] It is a good practice to compare the results obtained from the Sqrt(t) and G-function analyses for consistency.

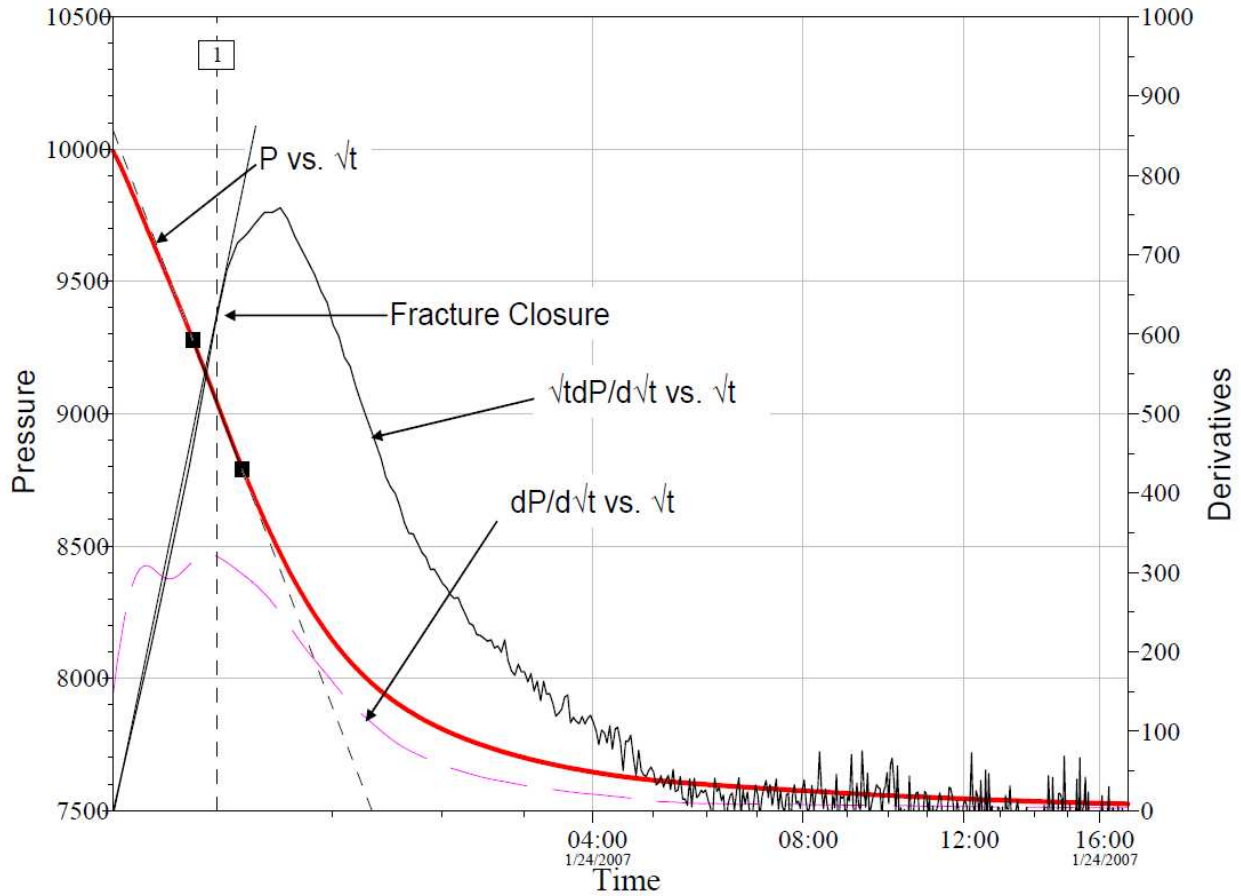


Figure 2.3 An example of Sqrt(t) Plot (Barree et al. 2007).

2.2.3 Log-Log Pressure Derivative

The log-log plot which represents pressure change from ISIP versus shut-in time is another diagnostic plot to estimate closure pressure. As shown by Figure 2.4 pressure difference and derivative curves are expected to display a parallel trend right before closure. The slope of these parallel lines can be used to diagnose the flow regime during the leakoff period before closure. The deviation of the pressure and derivative curves from the parallel trend marks up the fracture closure. Therefore, the log-log plot provides another means of verifying the estimation of fracture closure time and pressure from the G-function and Sqrt(t) analyses. Moreover, the semi-log

derivative curve after closure also indicates the flow regime present after closure with a slope of $(-1/2)$ or (-1) as seen on the Figure 2.4 (Barree et al. 2007).

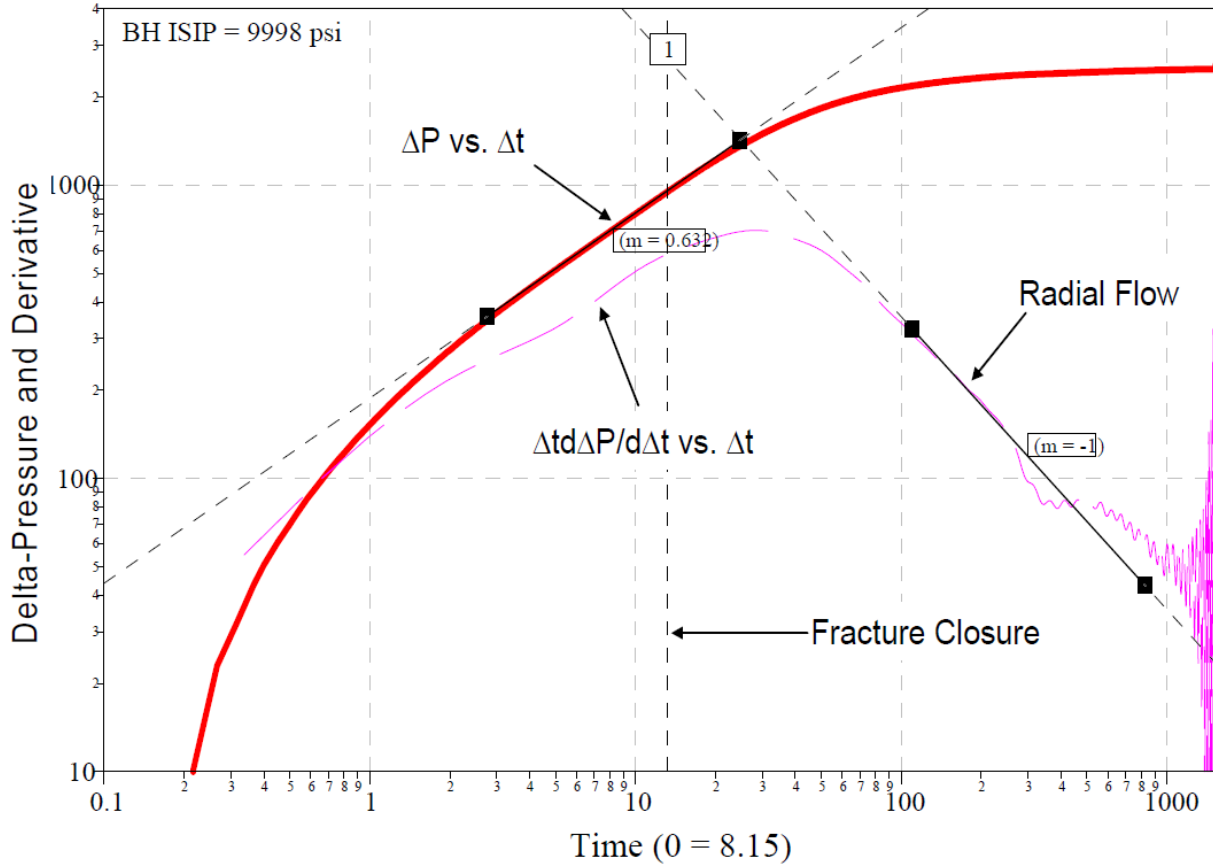


Figure 2.4 An example of Log-Log Plot (Barree et al. 2007).

2.2.4 After Closure Analysis (ACA)

After closure analysis (ACA) is performed to identify the flow regime after closure takes place. The flow regimes can be described using characteristic slopes on a log-log plot of monitored pressure difference which is defined as fall-off pressure minus pore pressure versus the square of the linear flow time function (F_L^2). The linear flow regime function (F_L) is described by Barree et al. (2007) as:

$$F_L(t, t_c) = \frac{2}{\pi} \sin^{-1} \sqrt{\frac{t_c}{t}} \quad \text{for } t \geq t_c \quad (2.11)$$

A typical ACA analysis is shown in Figure 2.5 where the slope of the semi-log derivative of pressure difference function indicates the existence of either pseudoradial or linear flow. In case of pseudolinear flow, the slope of the derivative curve on the log-log plot should be 0.5 whereas if pseudoradial flow exists, the slope of the derivative curve should be 1 (Barree et al. 2007). It is important to note that an initial guess of the reservoir pressure is needed to construct Figure 2.5; however, the slope of the semi-log derivative of the pressure difference function is independent of the reservoir pressure. If a pseudoradial flow period is identified, a Cartesian radial flow plot of monitored pressure during fall-off versus (F_L) or Horner plot can be used to determine the far-field transmissibility. However, there is a lot of controversy on whether a pseudoradial flow truly exists or not after closure.

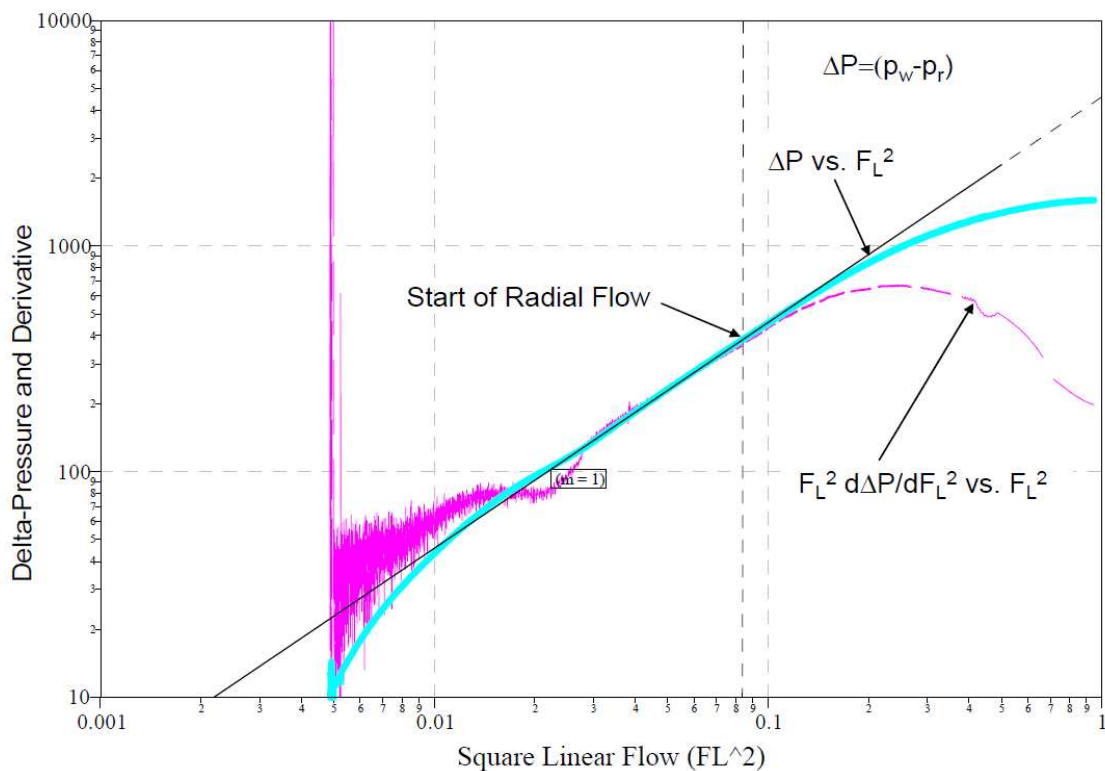


Figure 2.5 After Closure Analysis (ACA) Log Plot (Barree et al. 2007).

2.3 Typical Mistakes Encountered in DFIT Analysis

There are some common mistakes regarding the analysis of Diagnostic Fracture Injection Tests (DFITs). In this section, six of these common mistakes will be highlighted.

2.3.1 Incorrect Instantaneous Shut-in Pressure (ISIP) Determination

Correct determination of the Instantaneous Shut-in Pressure (ISIP) is extremely important because it is an important parameter for fracture treatment design and modeling. ISIP is determined during the analysis of pressure fall-off data and considered as a representative of the fracture-extension pressure. The difference between ISIP and closure pressure is called either net pressure or process zone stress, which is the resistance that the rock puts up to the fracture extension. Additionally, it is known that the net pressure has a control over the fracture width and height. The ISIP is not always clearly identified and does not happen right after shut-in. The fundamental reasons underlying the fact that ISIP does not occur right after shut-in are related to frictional pressures losses (pressure losses due to tortuosity and perforation), wellbore storage as well as decompression of the wellbore fluids. These factors have an impact on the amount of the continued injection taking place after shut-in. Besides, the continued injection after shut-in can take place for several minutes with the help of decompression and wellbore storage and can result in high pressure drops for especially large wellbore volumes, large pipe sizes as well as extended horizontal wells. Therefore, actual ISIP should be carefully chosen by extrapolating the pressure versus log of time curve back to the point at which shut-in occurs as seen in Figure 2.6.

Test Events

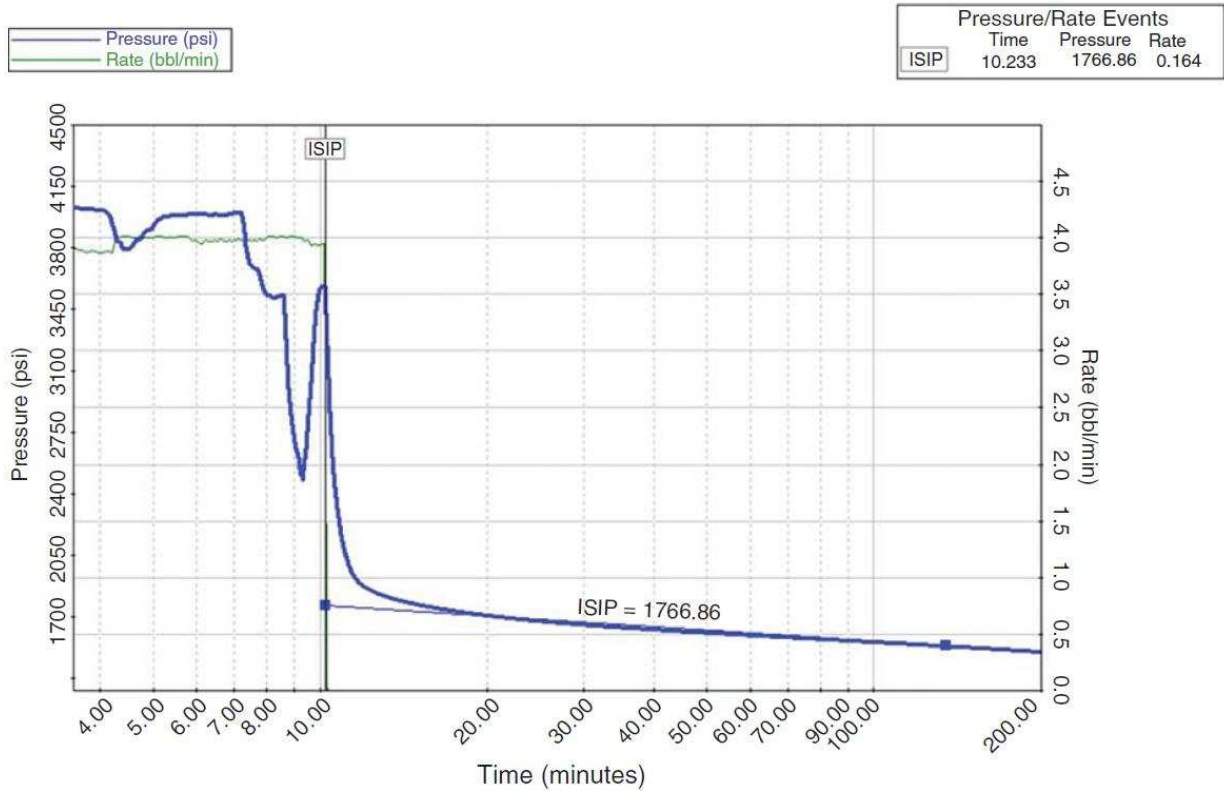


Figure 2.6 Extrapolation of the pressure versus log of time to find actual ISIP (Barree et al. 2015).

2.3.2 Selection of Closure Point

Selecting the closure point correctly is very important because it affects the interpretation of the test results and the estimation of flow capacity as well as post fracture production. Moreover, the error made in the closure stress will also affect the net pressure estimation, which is critical for fracture treatment design. Figure 2.7 shows examples of incorrect and correct determinations of closure point. To sum up, if the closure point is not chosen correctly, it will influence the accuracy validity of the DFIT analysis.

the rock to reach its ultimate dilation capacity. This undermines the creation of secondary shear fractures and affects the fracture height, leakoff rate, leakoff mechanism and reservoir permeability. Therefore, a high enough injection rate and correct injection time should be selected in order to have a valid DFIT analysis.

2.3.4 Phase Segregation and Gas Entry

Gas entry from the formation can happen during the fall-off period. For the ideal case of a sealed wellbore under isothermal conditions, the volume of gas bubbles remains the same while they rise to the surface. In addition to this, there is no mass transfer from the gas to the wellbore fluid and the moles of gas in the bubble stay constant; hence, the bubble pressure do not change in case of gas rising up to the surface. This will cause the perforation pressure to be doubled. Besides, the increase in the pressure caused by the rising gas bubble will increase the leakoff rate and the gas might dissolve in the wellbore fluid depending on the temperature change during its flow. Figure 2.8 shows an example of gas entry during the fall-off period for an actual treatment case.

2.3.5 Loss of Hydrostatic Head

The loss of the hydrostatic head invalidates the DFIT analysis. In most cases, wells do not go on vacuum at the surface nor do they lose the hydrostatic head. This means that the acquired surface pressure data exactly represents the down-hole pressures. However, when there is the loss of the hydrostatic head or presence of vacuum at the surface, after some time during the test, the surface pressure is no longer the representative of down-hole pressure, which makes the DFIT data unanalyzable. In order to prevent these problems, low-density fluid, bottom-hole gauge, or bottom-hole shut-in tools can be used.

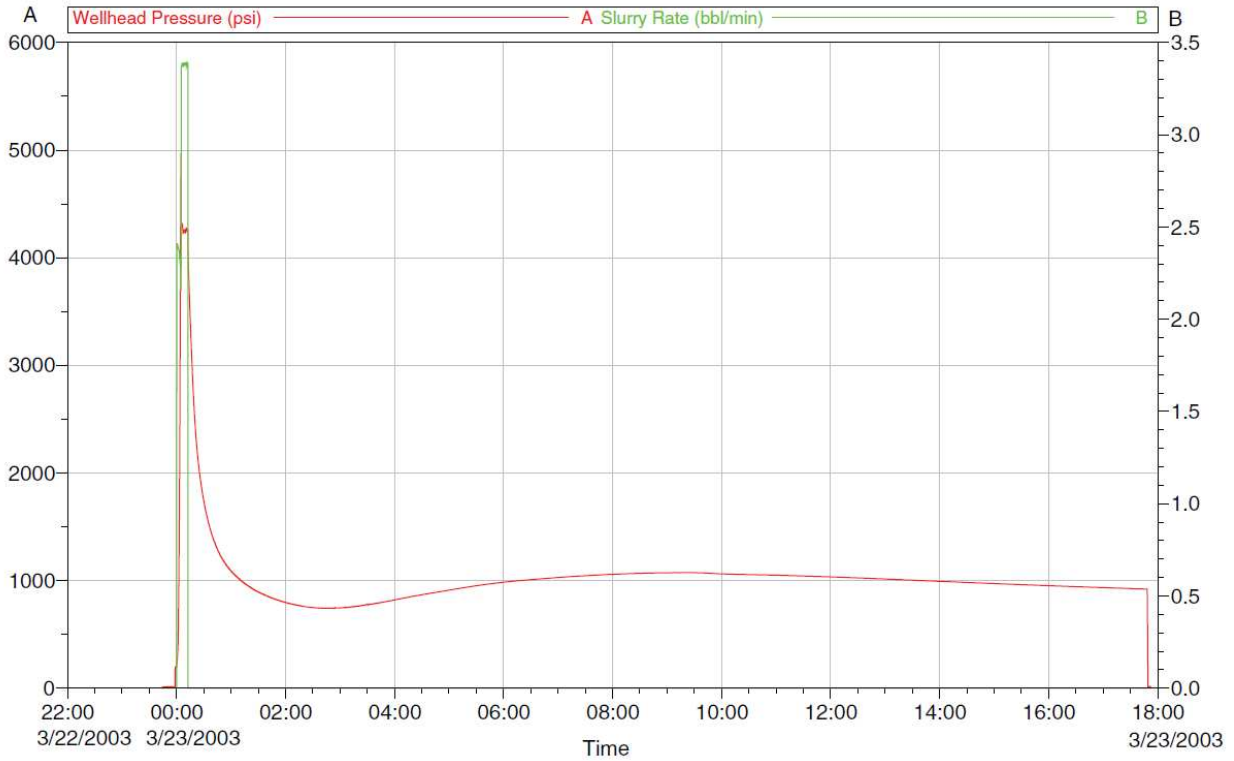


Figure 2.8 An example of gas-entry during the fall-off period for an actual treatment case (Barree et al. 2015).

2.3.6 Design of Test Duration

When pumping times become longer, there is more time for the pressure transient to penetrate within the zone of interest. The time for the fracture with a stable geometry to be closed is controlled by the reservoir permeability. The following equation represents an empirical approach to estimate the closure time required for the fracture:

$$t_c = \frac{t_p}{3k} \quad (2.11)$$

where,

t_c = the time to reach the fracture closure, min

t_p = the pumping time, min

k = the permeability of the leakoff system related to the fracture face, md

Figure 2.9 shows the estimated closure times with respect to pumping times and system permeabilities. Fracture closure can be accomplished with increasing pumping times for high permeability systems; nevertheless, when we increase the pumping times, fracture closure may take days to occur for low permeability systems such as unconventional reservoirs.

In the case of evaluating reservoir flow regime from the log-log plot of pressure change versus shut-in time, we need to wait three times longer than the closure time after shut-in (Barree et al. 2007). This time is needed for the reservoir transient flow to be established after the fracture closure. The time for the reservoir transient flow to be established is shown on an example in Figure 2.10, in which the pseudolinear flow is identified by a straight-line trend with slope of (-1/2) (Barree et al. 2007).

As discussed before, the possibility of having a pseudoradial flow regime after closure is very slim for unconventional reservoir systems (Barree et al. 2007). Equation 2.12 given below developed by Cinco-Ley and Samaniego (1981) can be used to estimate the time required for the pseudoradial flow to develop (Barree et al. 2015). Also the value of $t_{D_{xf}}$ must be at least equal to 1 during the fall-off period in case of a pseudoradial flow according to Cinco-Ley and Samaniego (1981),

$$t_{pr} = \frac{\phi \mu c_t x_f^2 t_{D_{xf}}}{0.0002637 k} \quad (2.12)$$

Where,

t_{pr} = the time to reach the pseudoradial flow, hours

ϕ = porosity, fraction

μ = the fluid viscosity, cp

x_f = the fracture half length, ft

C_t = total reservoir compressibility, 1/psi

k = the permeability of the leakoff system related to the fracture face, md

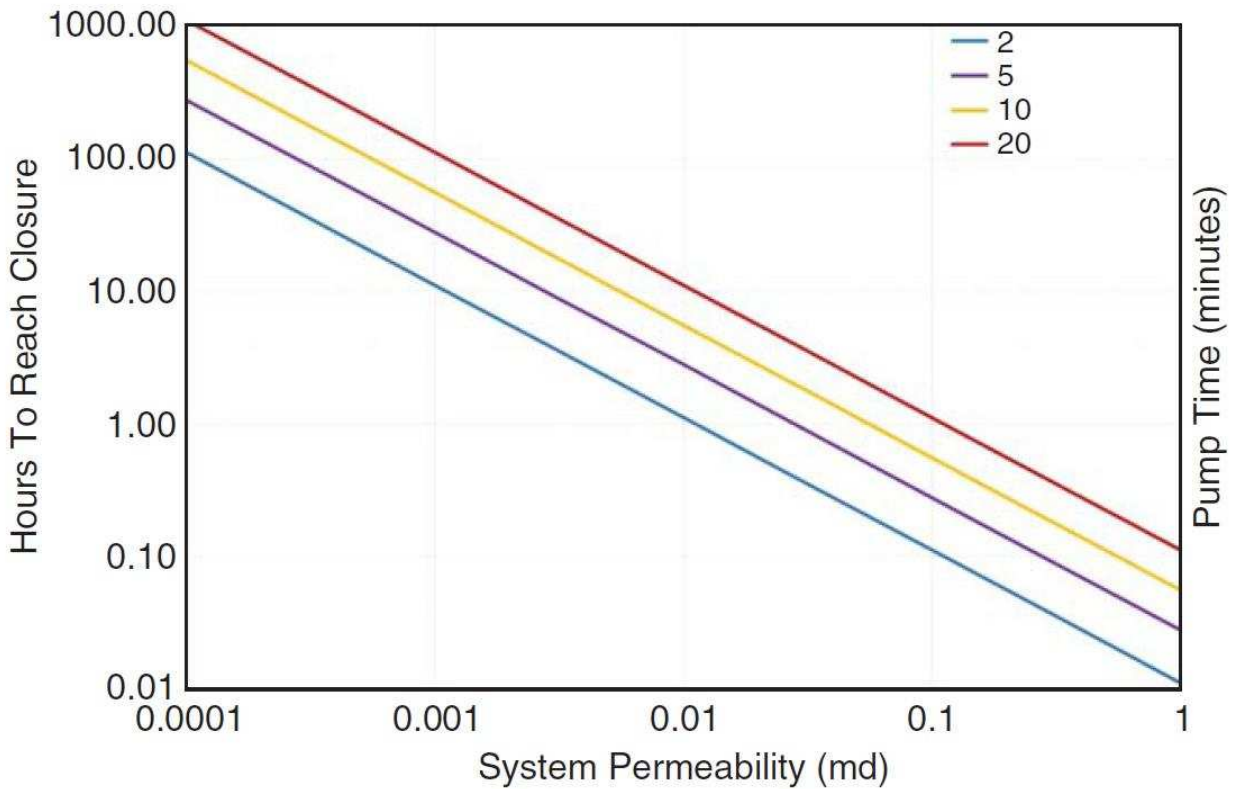


Figure 2.9 An example of the estimated time for the fracture closure depending on both pumping time and system permeability (Barree et al. 2015).

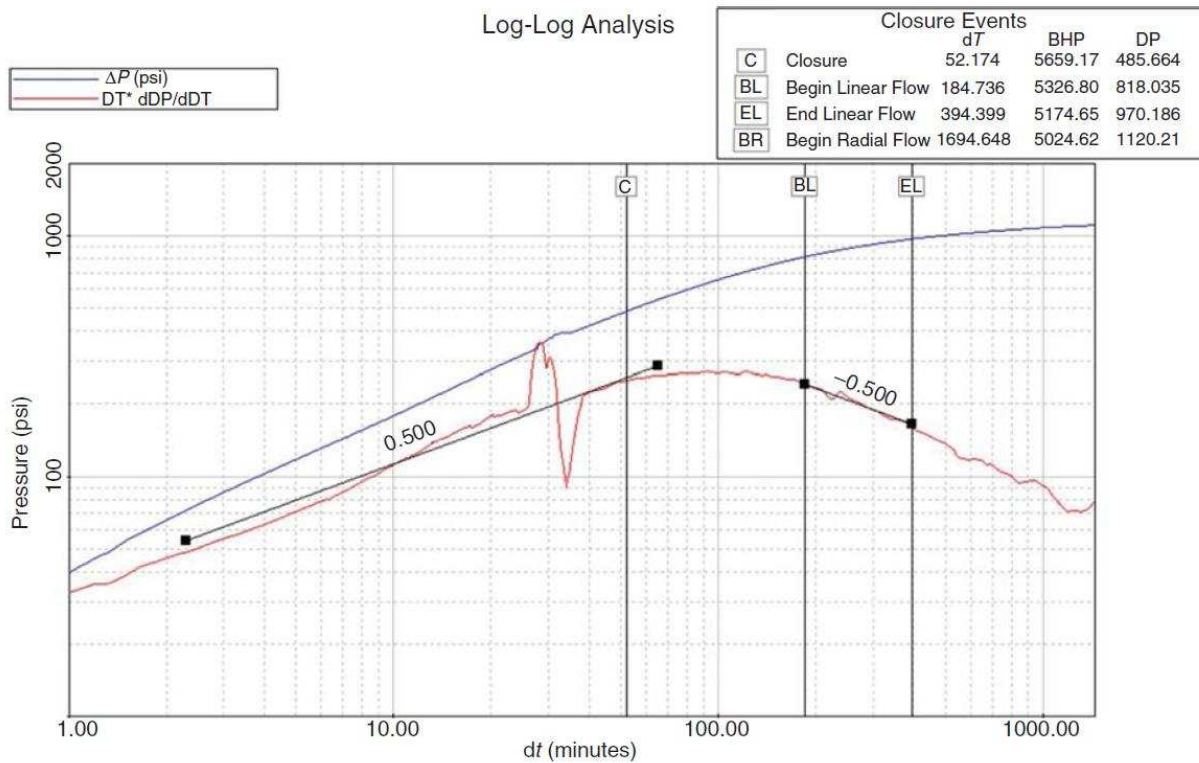


Figure 2.10 The log-log plot of pressure change versus shut-in time (Barree et al. 2015). When we consider a DFIT test in a system with 0.001 md with a pumping time of 5 minutes at 10 bbl/min and $t_{D_{xf}} = 1$, the time for the pseudoradial flow to start is nearly 1000 days of shut-in for a fracture half-length of 500 ft. This means that getting a pseudoradial flow in a DFIT test for unconventional systems that have very low permeabilities is practically impossible.

In Equation 2.12, $t_{D_{xf}}$, dimensionless time, is also defined by

$$t_{D_{xf}} = \frac{\beta kt}{\phi \mu c_t x_f^2} \tag{2.13}$$

where,

$t_{D_{xf}}$ = dimensionless time

t = time, hours

$\beta=0.0002637$, unit conversion constant

However, it might be still possible to see the negative unit slope after closure on the log-log plot, which may be attributed to pseudoradial flow, even though it is practically impossible to have pseudoradial flow in DFITs for low permeability and high heterogeneity systems. The fundamental reason for this is still not clear, but it is thought to be the composite response due to the shape of the created complex fracture system as shown in Figure 2.11. In other words, the composite response from this a complex fracture network looks similar to the response that may be caused by radial flow. Consequently, if pseudoradial flow analysis is applied after closure based on this response by using techniques such as Cartesian radial flow analysis and Horner analysis, which are only valid with a fully developed pseudoradial flow, the system permeability and transmissibility will be overestimated.

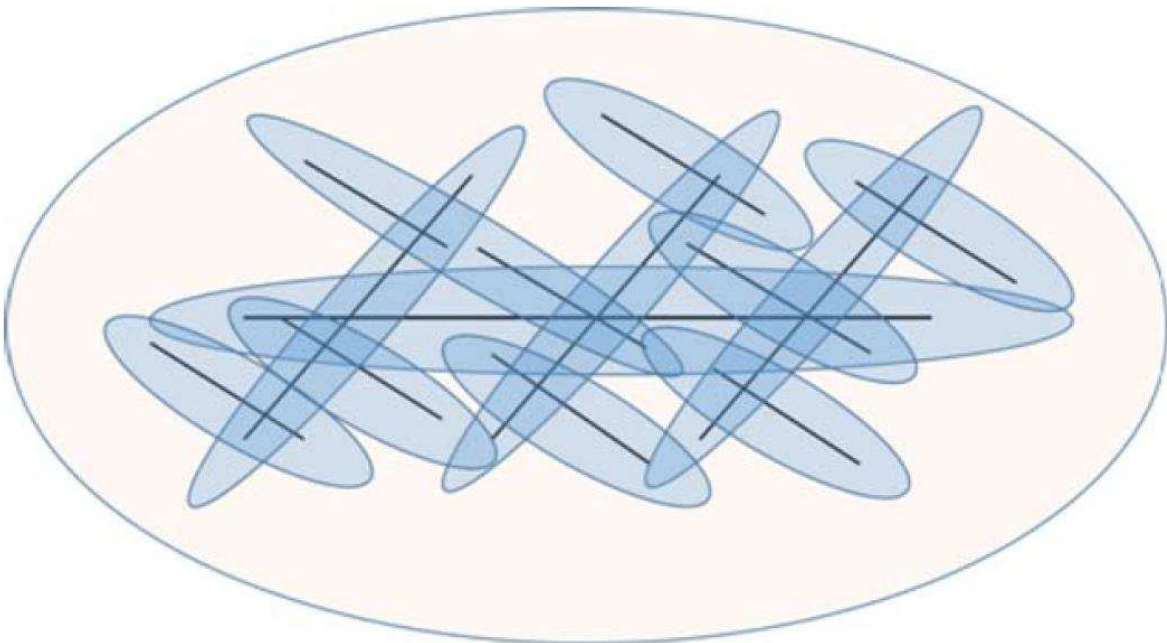


Figure 2.11 An example of the created complex fracture network (Barree et al. 2015).

CHAPTER 3

MATHEMATICAL MODELING

3.1 CFRAC model

CFRAC (Complex Fracturing ReseArch Code) is a discrete fracture network (DFN) simulator developed by McClure and Horne (2013) to carry out DFIT simulations. The simulator uses a finite volume element discretization and can create small or large hydraulic fractures within DFN.

In simulation, pore pressure, rock deformation, sliding velocity and direction, and the stress induced by the fracture deformation at each element are calculated at each simulation time step. Pressure, deformation, and void and hydraulic apertures are solved implicitly using the finite volume method. The Olson adjustment for leakoff is also applied to stress calculations in the pseudo 2D calculations (Jung 2015).

A significant feature of CFRAC, which is different from other hydraulic fracturing simulators, is the ability of allowing fractures to retain residual aperture after closure. Moreover, in CFRAC, the fractures can be categorized into two types: a hydraulic fracture and a preexisting fracture. Preexisting fractures exist at the beginning of the simulation. Hydraulic fractures form and propagate during the simulation.

CFRAC has two options for calculating fluid leakoff. The first is a one-dimensional fluid leakoff model, and the second is a fully numerical solution. The one-dimensional leakoff model developed by Vinsome and Westerveld (1980) was used in this study (Jung 2015).

Permeability (k) and transmissivity (T) of the fracture were defined according to the following equations (Jung 2015):

$$k_f = \frac{w^2}{12} \quad (3.1)$$

$$T = \frac{w^3}{12} \quad (3.2)$$

The fluid used in the simulations was isothermal, slightly compressible, liquid water with constant viscosity. Fluid flow calculations were based on the unsteady state mass balance and Darcy's law, given, respectively, by

$$\frac{\partial(\varepsilon\rho)}{\partial t} = -\nabla \cdot (q_{flux}e) - q_{leakoff} + s \quad (3.3)$$

$$q_{flux} = -\rho \frac{k}{\mu} \nabla P \quad (3.4)$$

where ε is the void aperture (the volume of fluid stored in the fracture divided by fracture surface area), e is hydraulic aperture (the volume divided by fracture surface area for fluid flow), t is time, q_{flux} is mass flux for the flow inside the fracture, s is a source term for a well, ρ is density, k is permeability, P is pressure, and $q_{leakoff}$ is leakoff rate from fracture surface area into the surrounding matrix.

The equation for aperture was based on its loading condition. The fractures were open when the walls were out of contact, because the fluid pressure became equal to the normal stress on the fracture, while fractures were closed if their walls were in contact and their fluid pressure was less than their normal stress. To calculate the aperture of closed fractures, CFRAC uses a joint closure relation developed by Barton et al. (1985) and Willis-Richards et al. (1996) expressed by

$$\varepsilon = \frac{E_0}{1+9\left(\frac{\sigma_n'}{\sigma_{n,Erref}}\right)} \quad (3.5)$$

where E_0 is the void aperture when the net pressure is equal to zero, and $\sigma_{n,Eref}$ is the pressure when the void aperture closes to 90% of E_0 . σ_n' is the effective normal stress, which is normal stress minus fluid pressure. In the simulations for this study, the void aperture is assumed to be equal to the hydraulic aperture. Eventually, The CFRAC program uses algorithms developed by Anderson et al. 1999, Amestoy et al. 1996, 2004, Bradley 2014, Dongarra et al. 1988, 1990, Davis 2004, 2006, Davis and Duff 1997, 1999, Guennebaud and Jacob 2010, Lawson et al. 1979, McClure et al. 2012, 2013, 2015, Craig and Jackson 2017.

3.1.1 Mechanical calculations

CFRAC is a fully numerical simulator that can simulate complex fracture networks. The boundary element method is used to perform mechanical calculations, which assumes elastically homogeneous, isotropic and linear elastic deformation, and small strain. The mechanical calculations converge to analytical solutions for fracture deformation (Sneddon 1946). The normal stress applied on a fracture was calculated using

$$\sigma_n' - P + \Delta\sigma_n = 0 \quad (3.6)$$

where σ_n' is the normal stress and $\Delta\sigma_n$ is the change in the normal stress due to back stress created by the deformation.

3.1.2 Fracture initiation and propagation

The direction and location of newly forming hydraulic fractures must be specified in advance. Hydraulic fracture initiation and propagation start from wellbore and the calculation follows linear elastic fracture mechanics. If the stress intensity factor exceeds the fracture toughness, the fracture will grow. The stress intensity factor (K_I), which was introduced by Olson

(2007), was calculated at the fracture tip elements according to

$$K_I = 0.806 \left(\frac{2G\sqrt{\pi}}{4(1-\nu)\sqrt{a}} \right) E_{open} \quad (3.7)$$

3.2 Simulation description

To better analyze DFIT data and estimate the formation permeability and closure pressure, four fundamental cases were investigated. Case 1 included only a homogeneous matrix and a newly forming hydraulic fracture with a fracture half-length of 10 m and residual aperture less than 500 micron. Case 2 was the same as case 1 except for the fact that the hydraulic fracture was allowed to have a residual aperture of 100 micron. Case 3 consisted of the same structure as Case 1; however the matrix permeability was increased. Finally, Case 4 included a homogeneous matrix with 1000 stochastically distributed natural fractures and a newly forming hydraulic fracture with a fracture half-length of 10 m and residual aperture less than 500 micron. Table 3.1 summarizes the simulation conditions for all four cases investigated.

Table 3.1 Fundamental simulation parameters for the four cases investigated

| Simulation Cases | Case 1 | Case 2 | Case 3 | Case 4 |
|----------------------------------|--------|--------|--------|--------|
| Hydraulic Fracture | x | x | x | x |
| Natural Fractures | | | | x |
| Matrix | x | x | x | x |
| Permeability, md | 0.0001 | 0.0001 | 0.01 | 0.0001 |
| Residual aperture, μm | <500 | 100 | <500 | <500 |

3.3 Fracture Geometries

Figures 3.1 and 3.2 show, respectively, the geometries of a single hydraulic fracture in a homogeneous matrix (Cases 1 through 3) and a hydraulic fracture in a naturally fractured (1000 fractures) matrix (Case 4). The black line in Figure 3.1 indicates the well. The red line in Figures

3.1 and 3.2 represents the newly formed hydraulic fracture. Stochastically distributed natural fractures are shown by the gray lines in Figure 3.2.

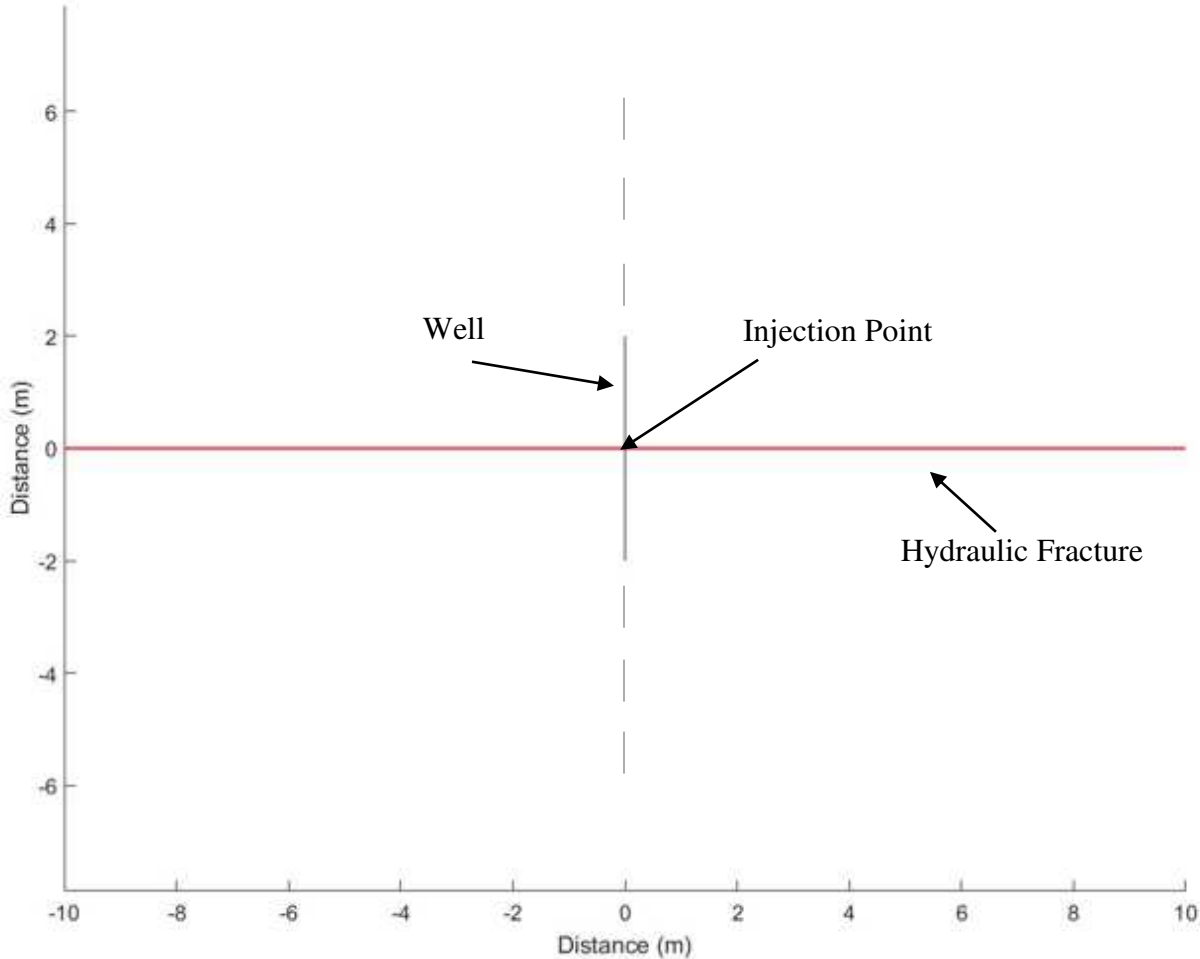


Figure 3.1 Hydraulic fracture geometry and dimension used for Cases 1, 2 and 3

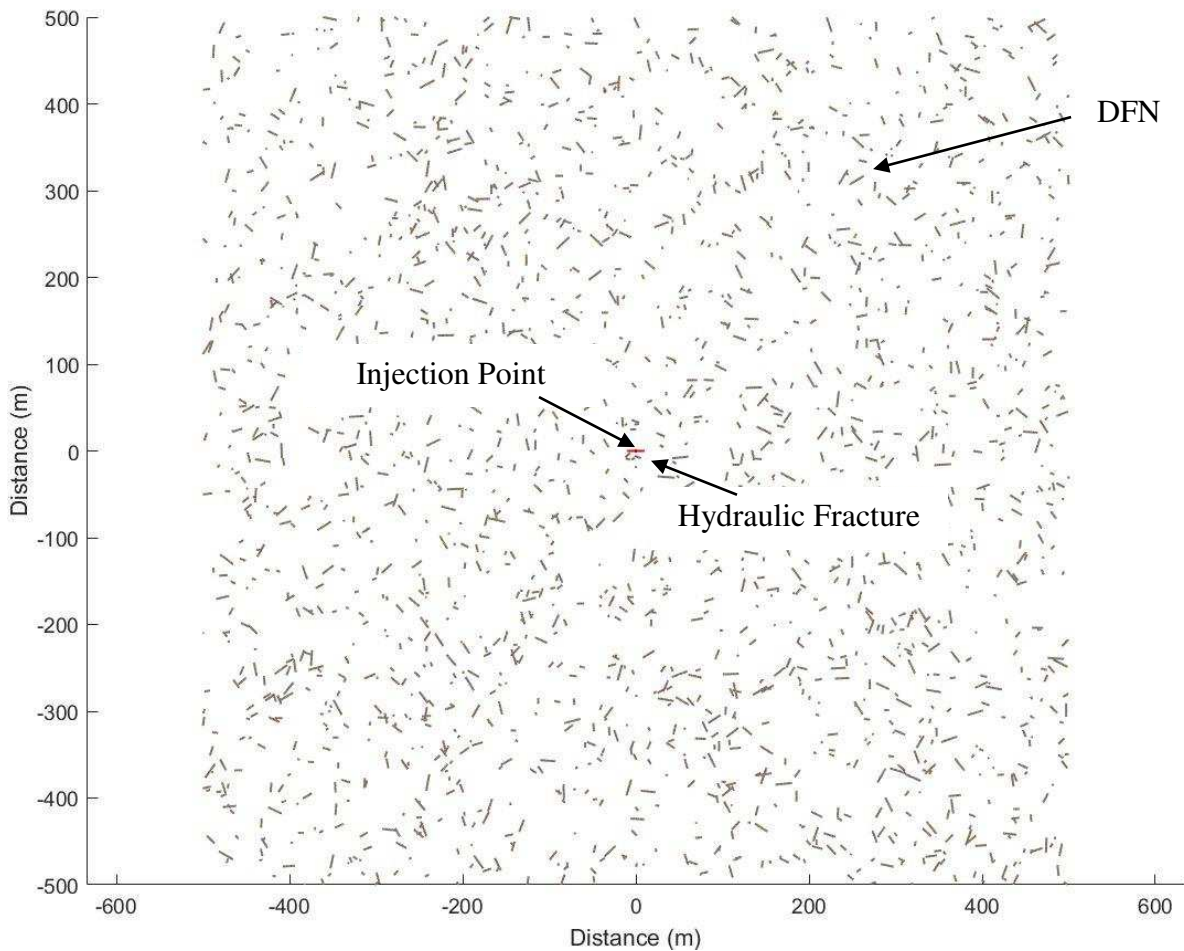


Figure 3.2 Discrete fracture network (DFN) and Hydraulic fracture (red) used for Case 4

3.4 Details of simulation parameters

The wellbore storage effect coefficient was 7.9797×10^{-4} bbl/psi. Initial reservoir pressure was 5076 psi. Perforation diameter was one inch, and there were 18 perforations. The injection rate was not constant over time and the maximum injection rate was 5 bbl/min for about 2 minutes. The simulation was continued after shut-in for about 35 days. Maximum residual aperture for the hydraulic fractures was assumed to be 500 micron. Shear modulus (G) was fixed at 15,000 MPa and Poisson's ratio (ν) was fixed at 0.25. The injected fluid was water with a constant viscosity of 1 cp. The fluid, rock and fracture compressibilities were 3.1578×10^{-6} 1/psi, 9.9974×10^{-6} 1/psi, and

6.89476×10^{-5} 1/psi, respectively. The matrix permeabilities were 0.0001 md for Cases 1, 2, and 4 and 0.01 md for Case 3. The matrix and fracture porosities were 0.3 and 0.00025, respectively. The storage ratio (r_p) was assumed to be 1 for Cases 1, 2 and 3, whereas it was assumed to be 0.9 for Case 4. Finally, the minimum horizontal stress was 8000 psi.

CHAPTER 4

RESULTS AND DISCUSSIONS

4.1 Simulation Results

This chapter presents the simulation results for the four cases described in Chapter 3. The results are analyzed by the G-function method and the direct application of Nolte's (1979, 1986, 1988) formulation to estimate matrix permeability.

4.1.1 Case 1

This case only included a homogeneous matrix and a newly forming hydraulic fracture with a fracture half-length of 10 m and residual aperture of less than 500 micron. Figure 4.1 shows the bottom-hole pressure and $G^*(dP/dG)$ with respect to G-time. From the figure, the instantaneous shut-in pressure and closure pressure are estimated to be around 7800 and 7140 psi, respectively. The closure took place when G time was equal to 45. Then, the G-function permeability was estimated from Equation 2.10 as follows:

$$k_m = 0.0086 * 1 * \frac{\sqrt{0.01*(7800-7140)}}{0.03*(13.1552*10^{-6})*\left(\frac{45*5.44*1}{0.038}\right)^{1.96}} = 0.001915 \text{ md}$$

Then, Δp was estimated by Equation 2.3 and plotted versus G in Figure 4.2. Figure 4.3 is the log-log plot of Δp versus G-time. A straight line was drawn through the data in Figure 4.3 with 0.5 slope, which is an indication of linear flow. The identified linear flow data in Figure 4.3 were replotted on Cartesian coordinates in Figure 4.4 and the resulting slope was calculated to be 8.7598.

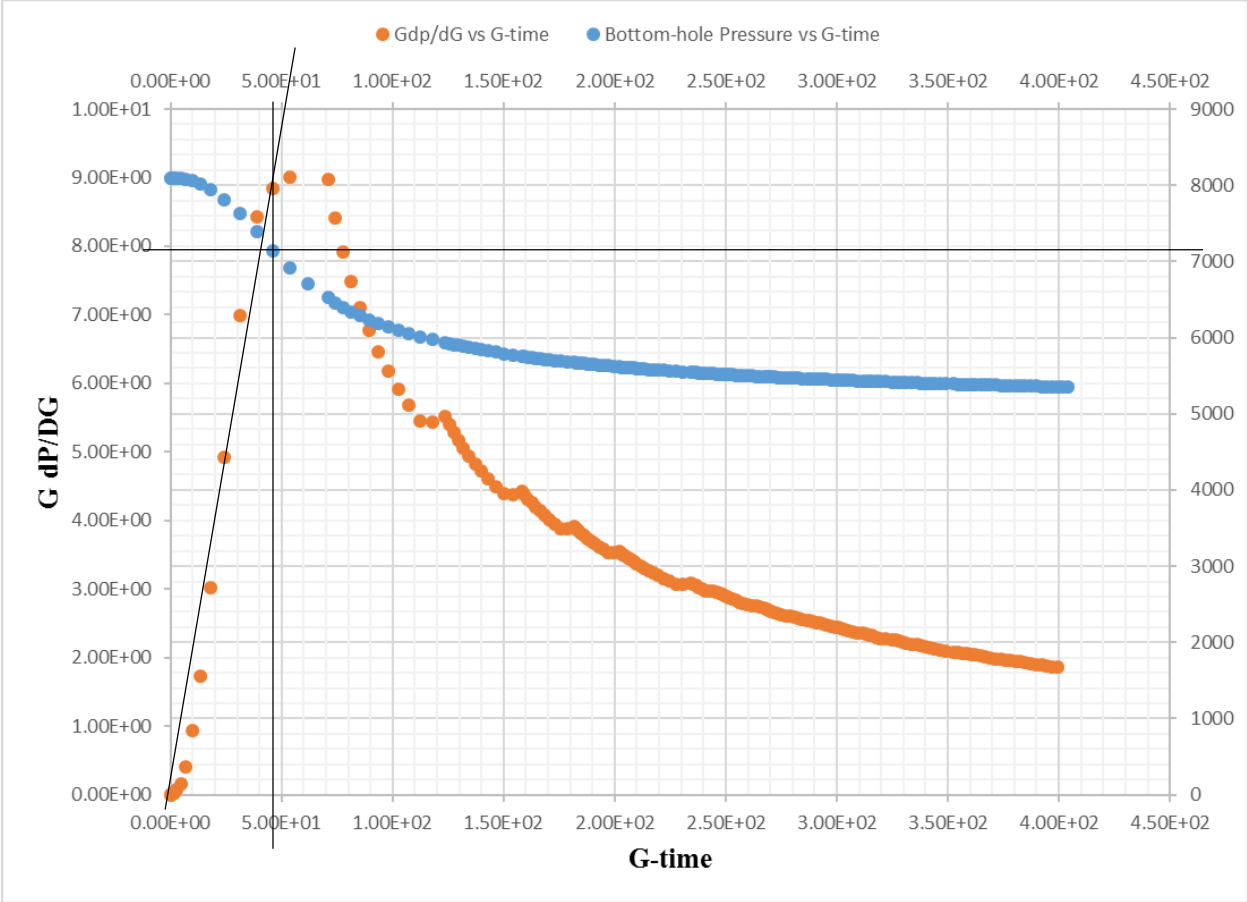


Figure 4.1 The G-function plot for Case 1

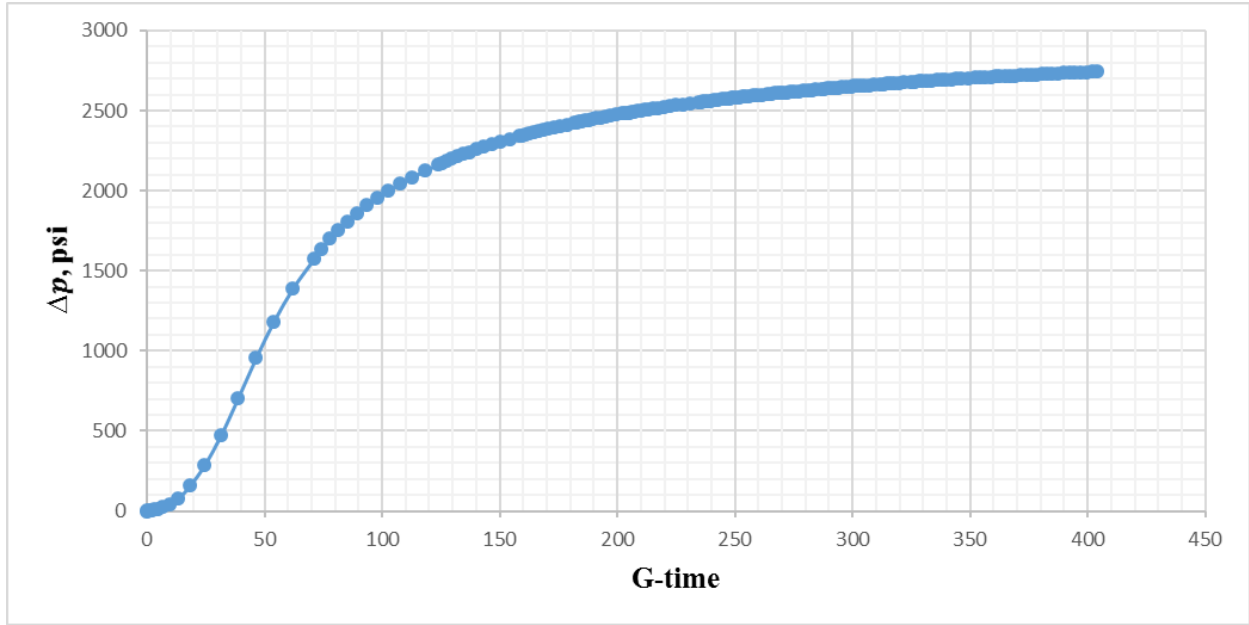


Figure 4.2 The plot of Δp versus G for Case 1

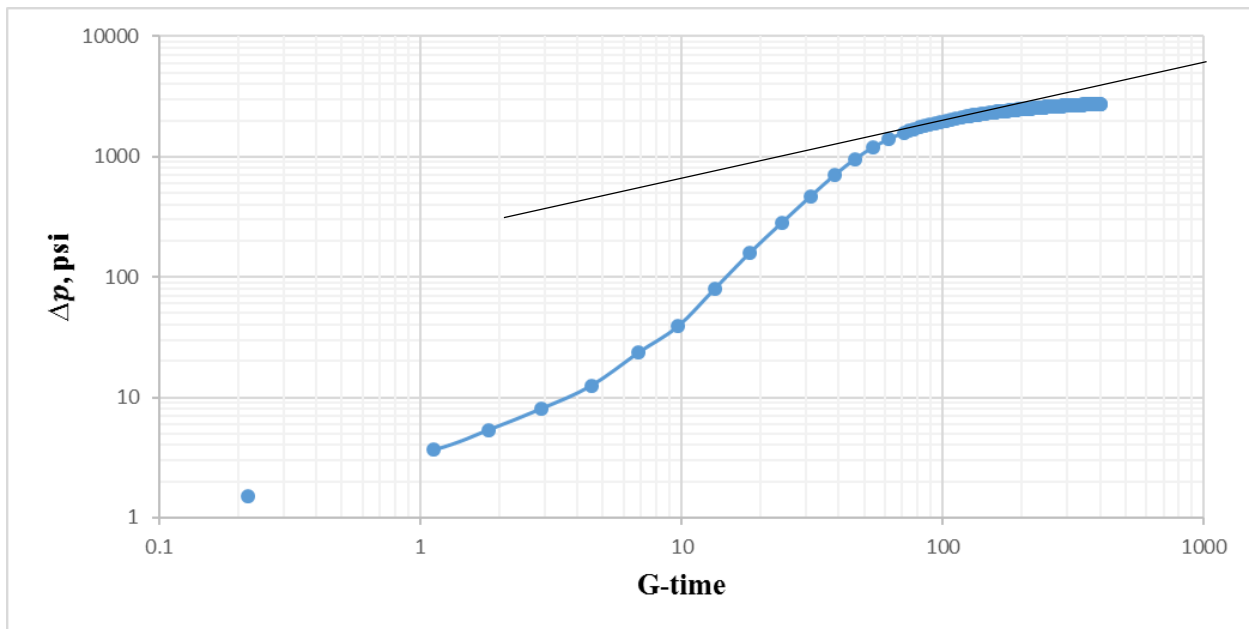


Figure 4.3 The log-log plot of Δp versus G for Case 1

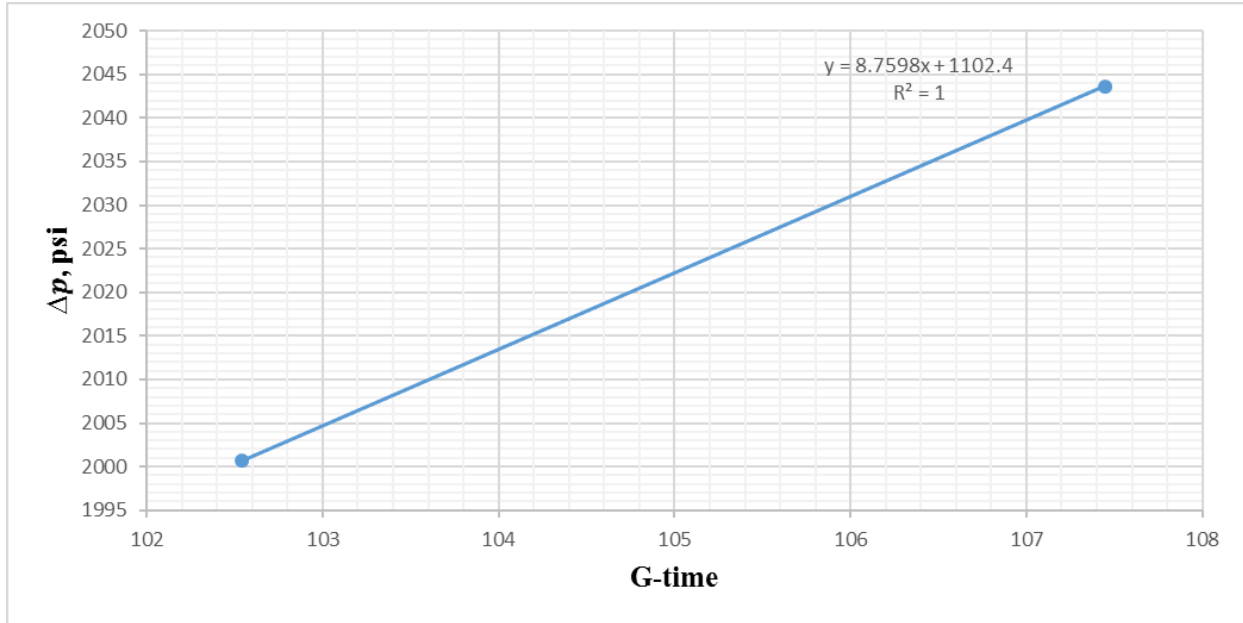


Figure 4.4 The plot of Δp versus G within the linear flow interval for Case 1

The leakoff coefficient was calculated using Equations 2.6 and 2.7 as follows

$$C_L = \frac{2 \left[\frac{\pi(1-\nu^2)}{2E} \right] x_f m}{\pi \sqrt{t_p}} = \frac{2 \left[\frac{\pi(1-0.25^2)}{2 * 5.44 * 10^{-6}} \right] * 32.81 * 8.7598}{\pi * \sqrt{2}} = 35.023 * 10^{-6} \text{ ft}/\sqrt{\text{min}}$$

and the matrix permeability was calculated from Equation 2.9 as

$$k_m = \frac{1 * (35.023 * 10^{-6})^2}{0.03 * (13.1552 * 10^{-6}) * (0.00118 * (7140 - 5076))^2} = 0.00052 \text{ md}$$

It is important to note that this permeability was calculated using the extended fracture half-length, which is the final half-length at the end of the simulation. We also calculated the permeability using the fracture half-length at closure which was 14.33 ft. This yielded

$$k_m = \frac{1 * (15.29 * 10^{-6})^2}{0.03 * (13.1552 * 10^{-6}) * (0.00118 * (7140 - 5076))^2} = 0.00009 \text{ md}$$

4.1.2 Case 2

This case was the same as Case 1 except for the residual aperture of the hydraulic fracture. One of Nolte's assumptions in his G-function formulation is that the fractures fully close and, in this case, the G-function permeability theoretically becomes equal to the matrix permeability. To test this assumption, in Case 2, a smaller aperture of 100 μm than Case 1 was considered.

Figure 4.5 shows the G-function analysis for this case, which yields an instantaneous shut-in pressure (ISIP) estimate of 8000 psi and closure pressure estimate of 7700 psi. Besides, the G closure time was determined to be 41.

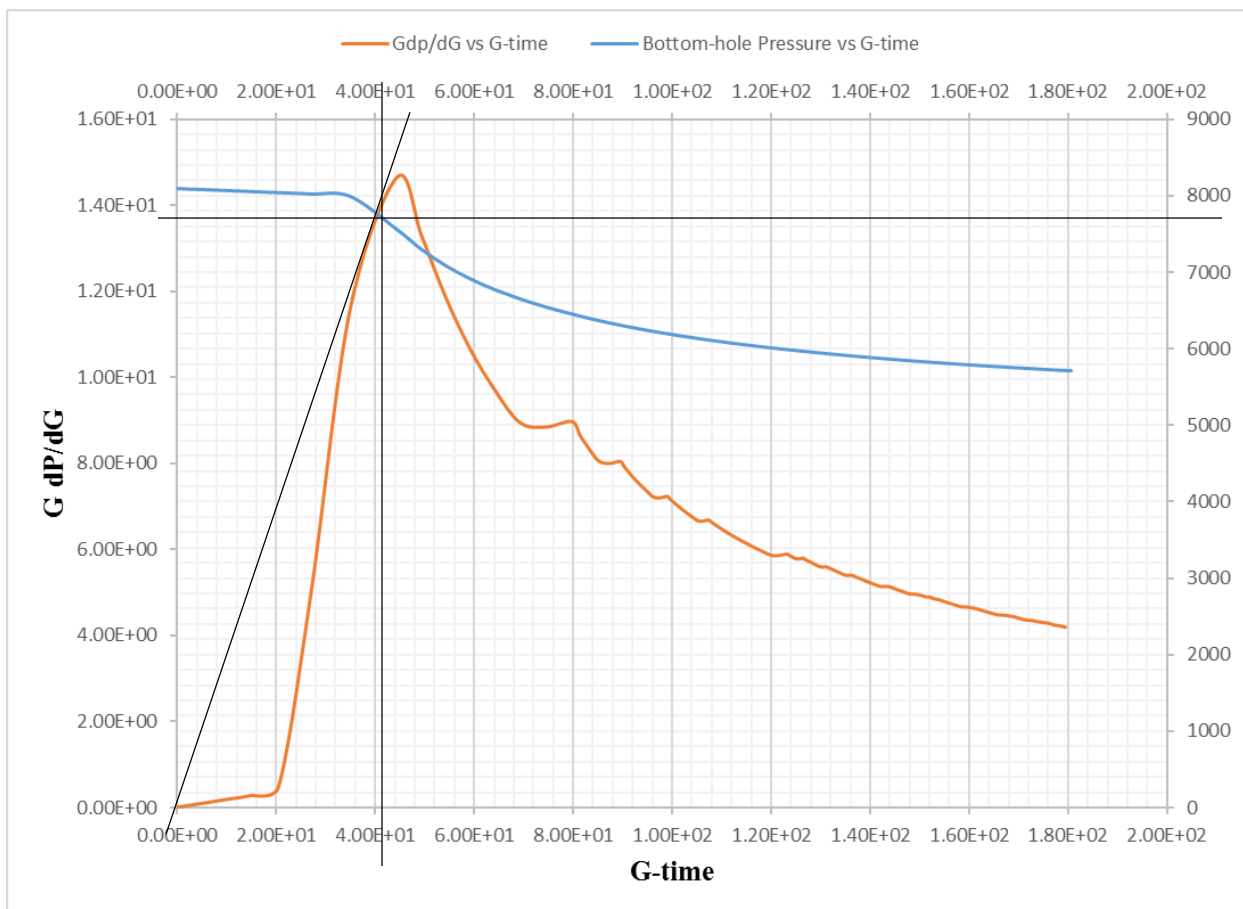


Figure 4.5 The G-function curve for Case 2

Using this information, the G-function permeability was estimated from Equation 2.10 as follows:

$$k_m = 0.0086 * 1 * \frac{\sqrt{0.01*(8000-7700)}}{0.03*(13.1552*10^{-6})*\left(\frac{41*5.44*1}{0.038}\right)^{1.96}} = 0.0015 \text{ md}$$

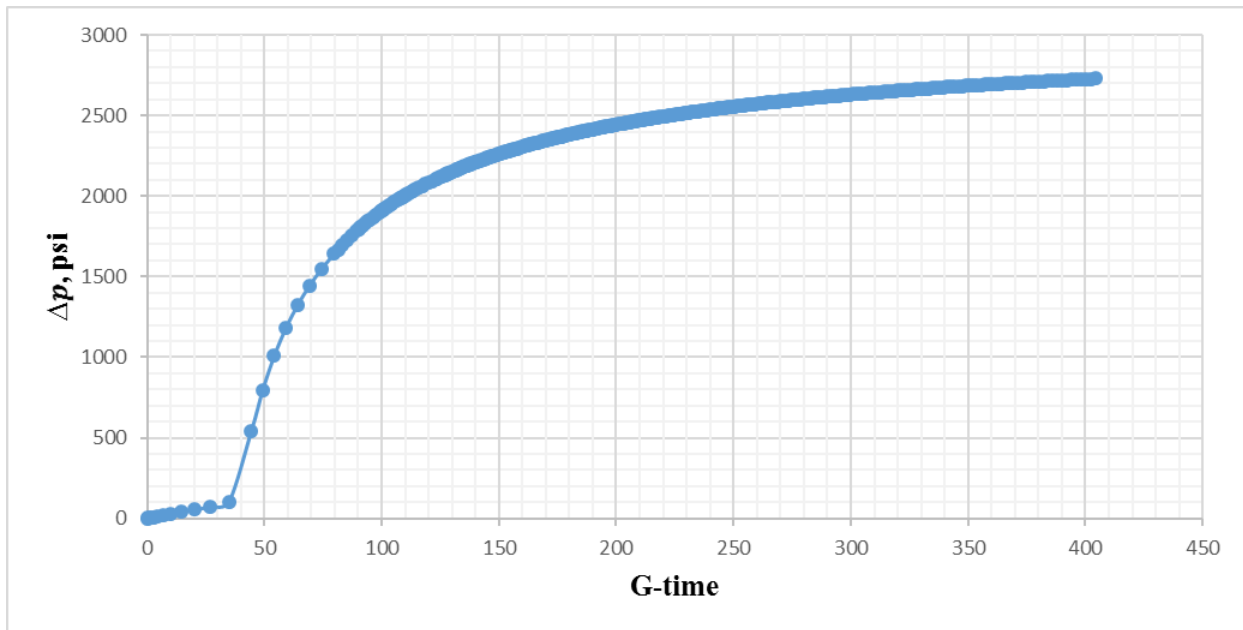


Figure 4.6 The plot of Δp versus G for Case 2

Similar to case 1, Δp was calculated through Equation 2.3 and plotted versus G in Figure 4.6. The log-log plot of Δp versus G-time shown in Figure 4.7 indicates a linear flow interval after closure as marked by the 0.5-slope straight line. The Cartesian plot of the linear flow data yields a straight line slope of 9.0462 as shown in Figure 4.8.

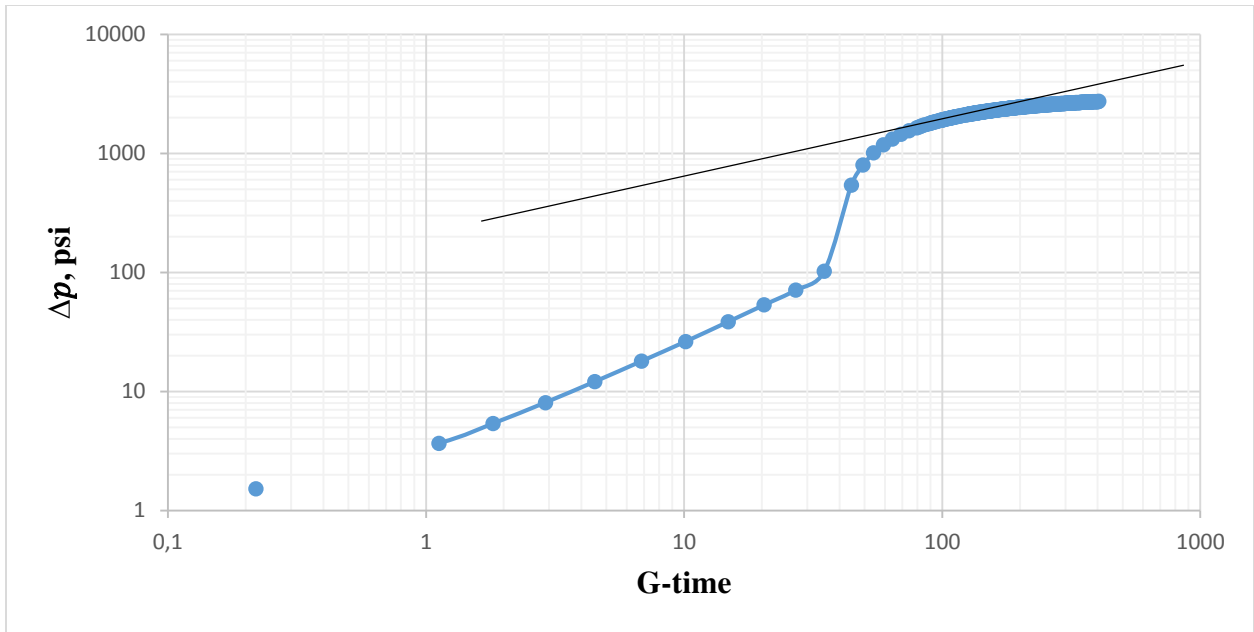


Figure 4.7 The log-log plot of Δp versus G for Case 2

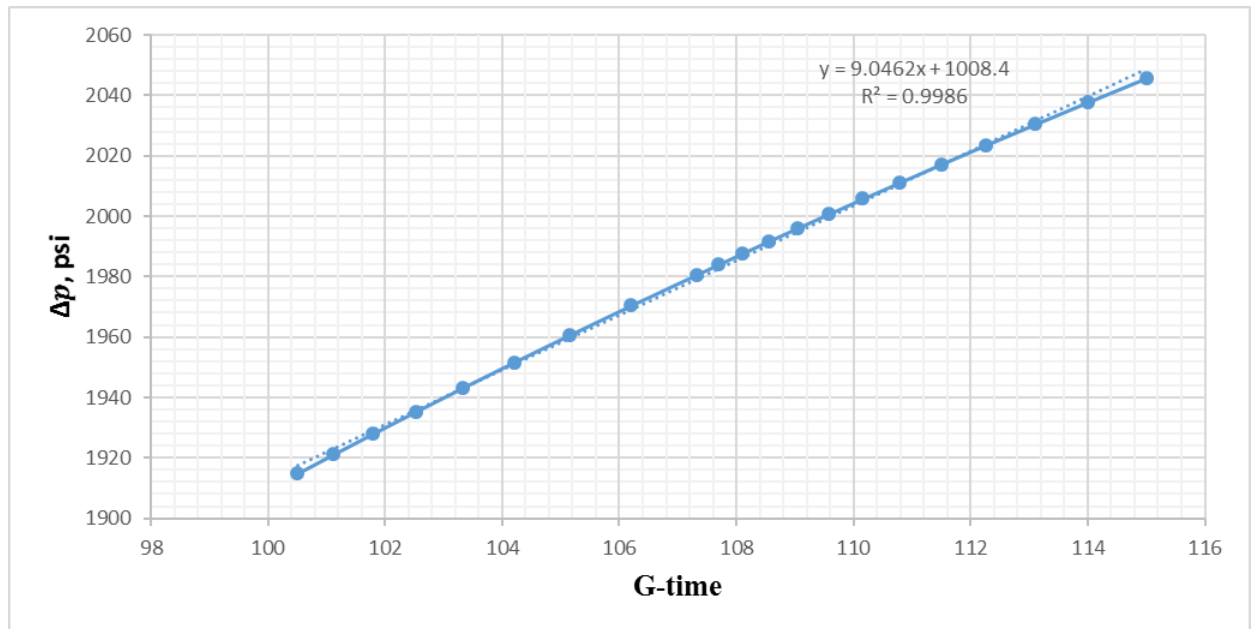


Figure 4.8 The plot of Δp versus G within the linear flow interval for Case 2

The leakoff coefficient is obtained from Equations 2.6 and 2.7 as follows:

$$C_L = \frac{2 \left[\frac{\pi(1-\nu^2)}{2E} \right] x_f m}{\pi \sqrt{t_p}} = \frac{2 \left[\frac{\pi(1-0.25^2)}{2 * 5.44 * 10^{-6}} \right] * 32.81 * 9.0462}{\pi * \sqrt{2}} = 36.168 * 10^{-6} \text{ ft}/\sqrt{\text{min}}$$

Using the extended fracture half-length yields a matrix permeability of

$$k_m = \frac{1 * (36.168 * 10^{-6})^2}{0.03 * (13.1552 * 10^{-6}) * (0.00118 * (7700 - 5076))^2} = 0.00035 \text{ md}$$

and the fracture half-length at closure (17.979 ft) leads to

$$k_m = \frac{1 * (19.82 * 10^{-6})^2}{0.03 * (13.1552 * 10^{-6}) * (0.00118 * (7140 - 5076))^2} = 0.0001038 \text{ md}$$

4.1.3 Case 3

For Case 3, the matrix permeability was increased to 0.01 md (compared to 0.0001 md for Cases 1 and 2) to understand the effect of higher permeability on the accuracy of the G-function analysis to estimate permeability and leakoff coefficient. The rest of the parameters were kept the same as they were in Case 1. Figure 4.9 indicates a G-closure time a 2.6. Additionally, the closure pressure was found to be 7400 psi while the instantaneous shut-in pressure was 8000 psi. Based on the results of the G-function analysis, matrix permeability was calculated as follows

$$k_m = 0.0086 * 1 * \frac{\sqrt{0.01 * (8000 - 7400)}}{0.03 * (13.1552 * 10^{-6}) * \left(\frac{2.6 * 5.44 * 1}{0.038} \right)^{1.96}} = 0.488 \text{ md}$$

Figure 4.10 shows the calculated Δp versus G-time plot and Figure 4.11 is the log-log plot of Δp versus G-time. A $\frac{1}{2}$ -slope straight line can be fit through the data in Figure 4.11 indicating a linear flow period. The same linear flow data was plotted on Cartesian coordinates as shown in Figure 4.12 which yielded a slope of 49.176.

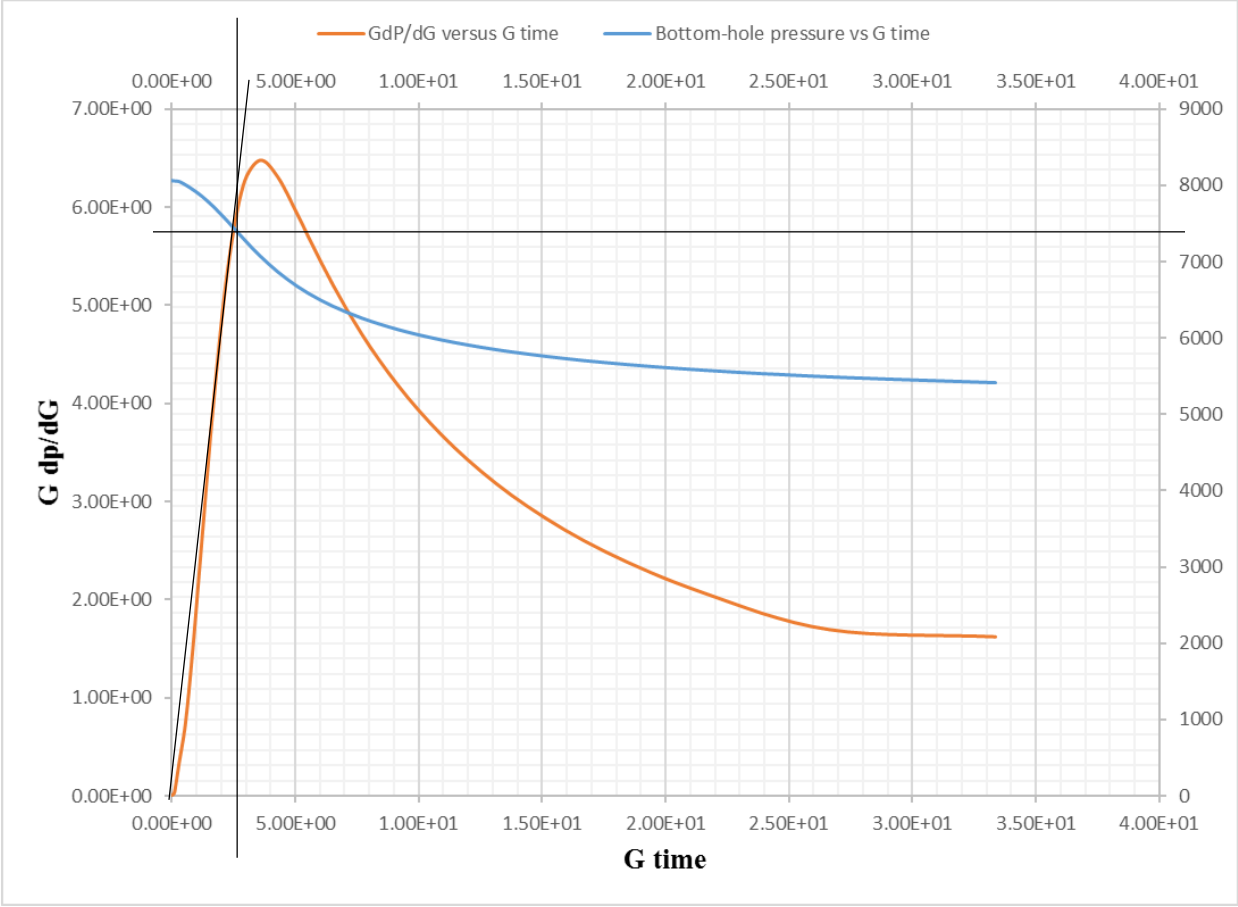


Figure 4.9 The G-function curve for Case 3

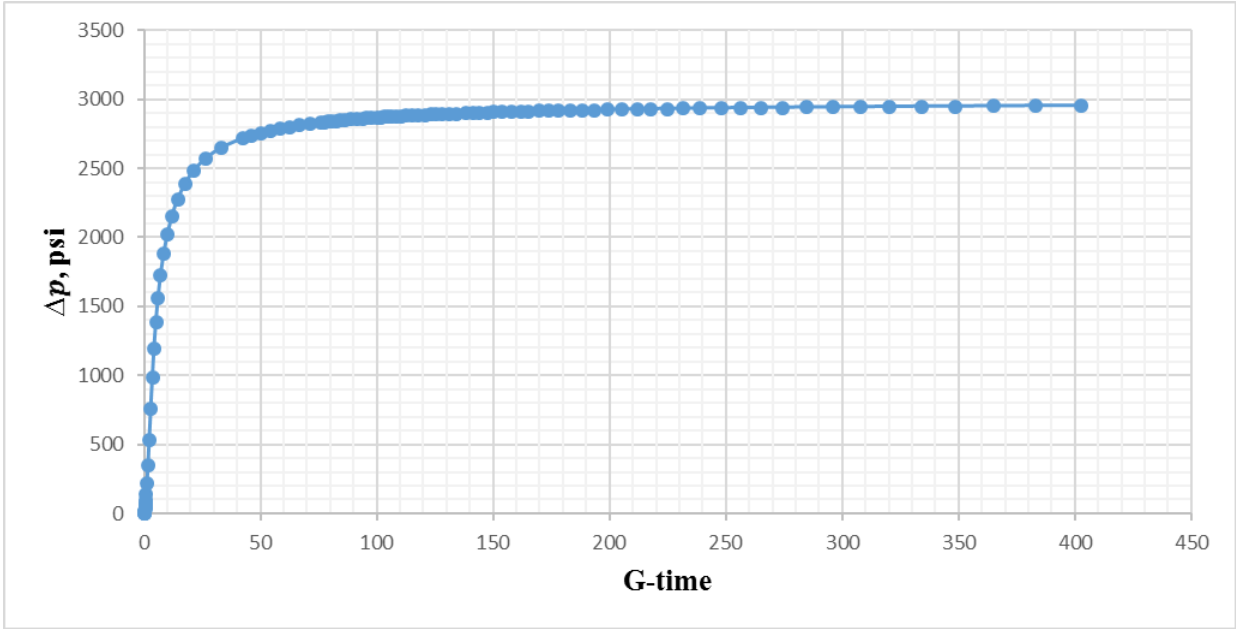


Figure 4.10 The plot of Δp versus G for Case 3

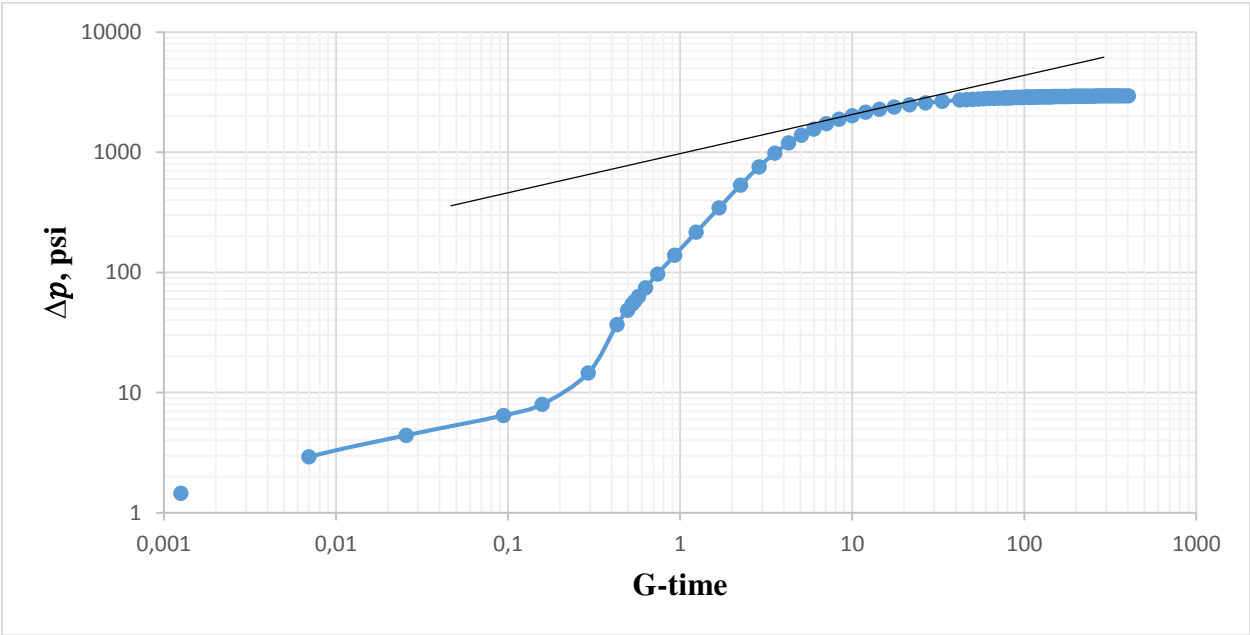


Figure 4.11 The log-log plot of Δp versus G for Case 3

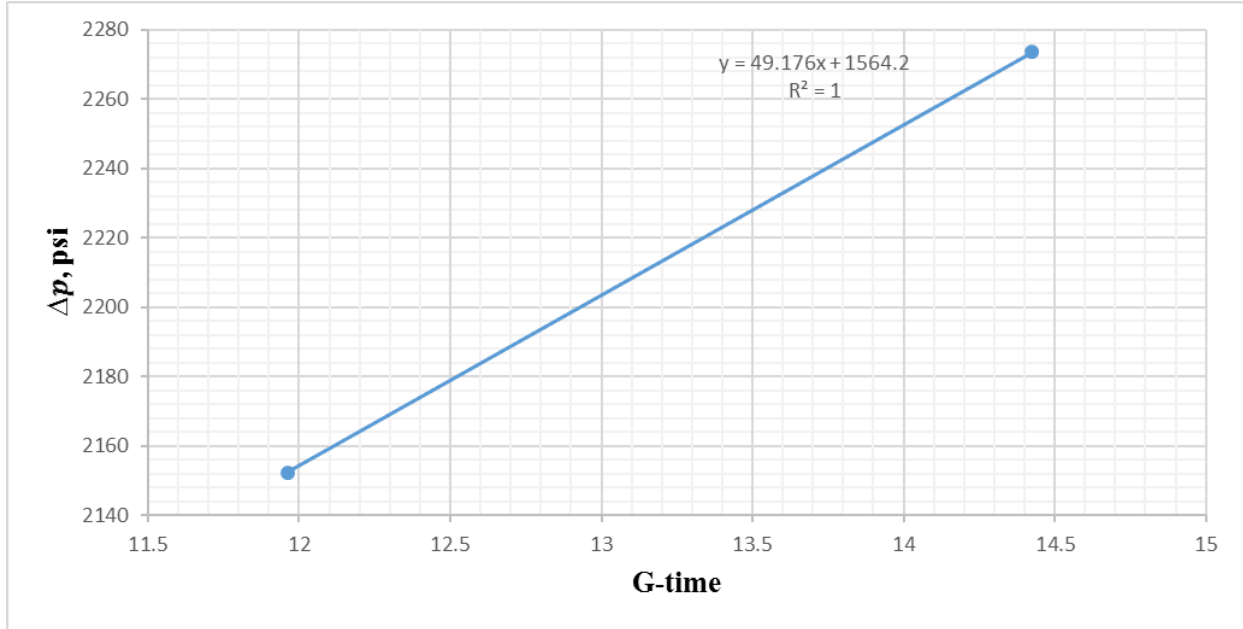


Figure 4.12 The plot of Δp versus G within the linear flow interval for Case 3

Based on this information, the leakoff coefficient is obtained from Equations 2.6 and 2.7 as follows:

$$C_L = \frac{2 \left[\frac{\pi (1-\nu^2)}{2E} \right] x_f m}{\pi \sqrt{t_p}} = \frac{2 \left[\frac{\pi (1-0.25^2)}{2 * 5.44 * 10^{-6}} \right] * 32.81 * 49.176}{\pi * \sqrt{2}} = 196.6150 * 10^{-6} \text{ ft}/\sqrt{\text{min}}$$

Moreover, the matrix permeability, using the extended fracture half-length, was estimated as

$$k_m = \frac{1 * (196.6150 * 10^{-6})^2}{0.03 * (13.1552 * 10^{-6}) * (0.00118 * (7400 - 5076))^2} = 0.013 \text{ md}$$

On the other hand, the fracture half-length at closure (28.74 ft) yields

$$k_m = \frac{1 * (177.225 * 10^{-6})^2}{0.03 * (13.1552 * 10^{-6}) * (0.00118 * (7140 - 5076))^2} = 0.01 \text{ md}$$

4.1.4 Case 4

This case was intended to investigate the effect of complex fracture network on the estimation of G-function permeability and leakoff coefficient. It included 1000 stochastically distributed natural fractures, a homogeneous matrix, and a newly forming hydraulic fracture with a half-length of 10 m and residual aperture less than 500 μm . Figure 4.13 shows the G-function plot for this case, which indicates a G-closure time of 36. The corresponding closure pressure is 7410 psi while the instantaneous shut-in pressure is 7810 psi.

The calculation of G-function permeability requires the use of total porosity-compressibility product, $(\phi c_t)_{f+m}$:

$$(\phi c_t)_{f+m} = \phi_f * (c_t)_f + \phi_m * (c_t)_m$$

$$(\phi c_t)_{f+m} = 0.00025 * (3.1578 * 10^{-6} + 6.89476 * 10^{-5})_f + 0.03 * (3.1578 * 10^{-6} + 9.9974 * 10^{-6})_m$$

$$(\phi c_t)_{f+m} = 0.0000004127 \text{ psi}^{-1}$$

Using $(\phi c_t)_{f+m}$, the G-function permeability is calculated as follows:

$$k_m = 0.0086 * 1 * \frac{\sqrt{0.01 * (7810 - 7410)}}{0.0000004127 * \left(\frac{36 * 5.44 * 0.9}{0.038}\right)^{1.96}} = 0.0027 \text{ md}$$

Similar to the other cases, calculated Δp versus G-time was plotted in Figure 4.14. The log-log plot of Δp versus G in Figure 4.15 indicates a linear flow period after closure. The Cartesian plot of the linear flow data shown in Figure 4.16 yields a slope of 9.5197.

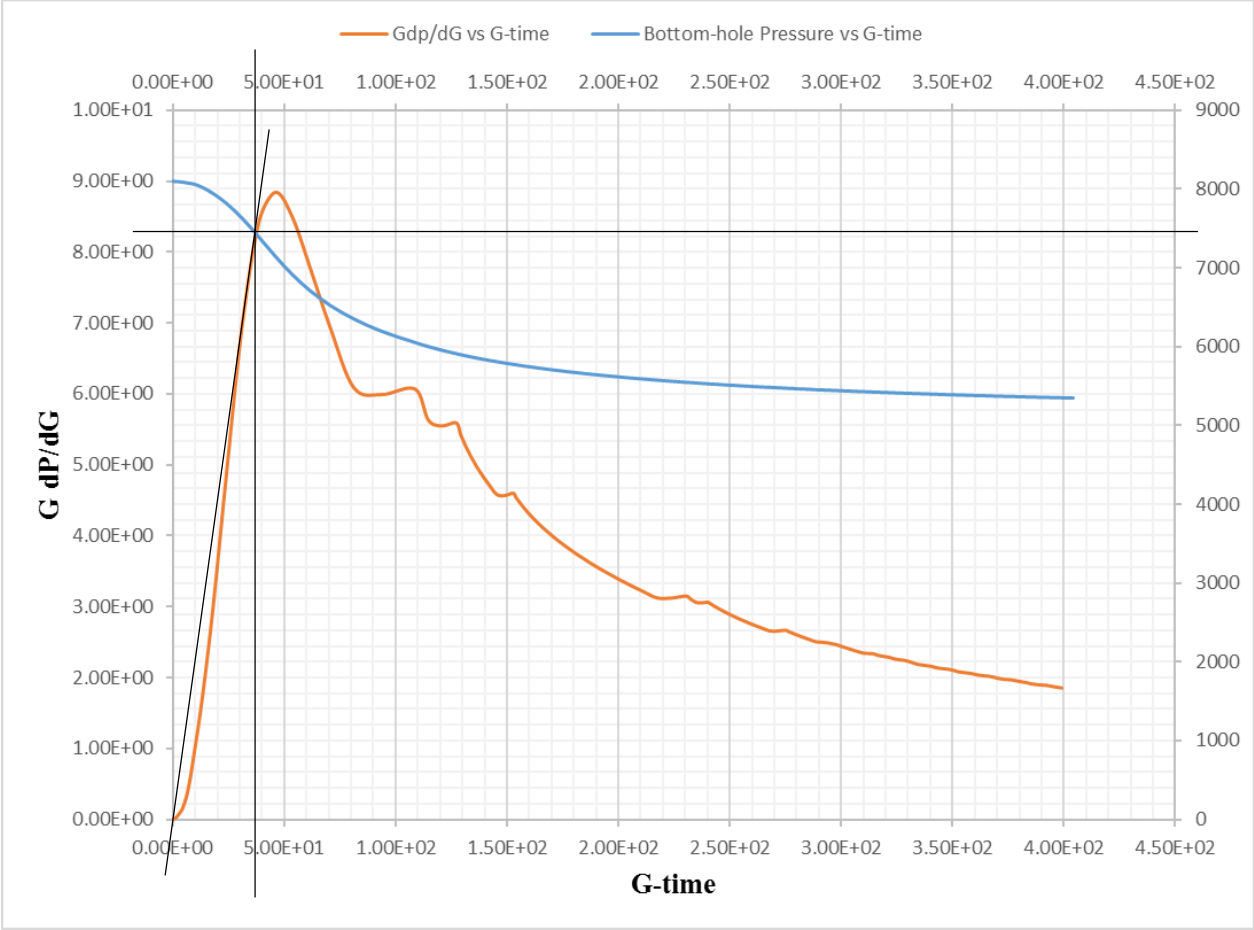


Figure 4.13 The G-function curve for Case 4

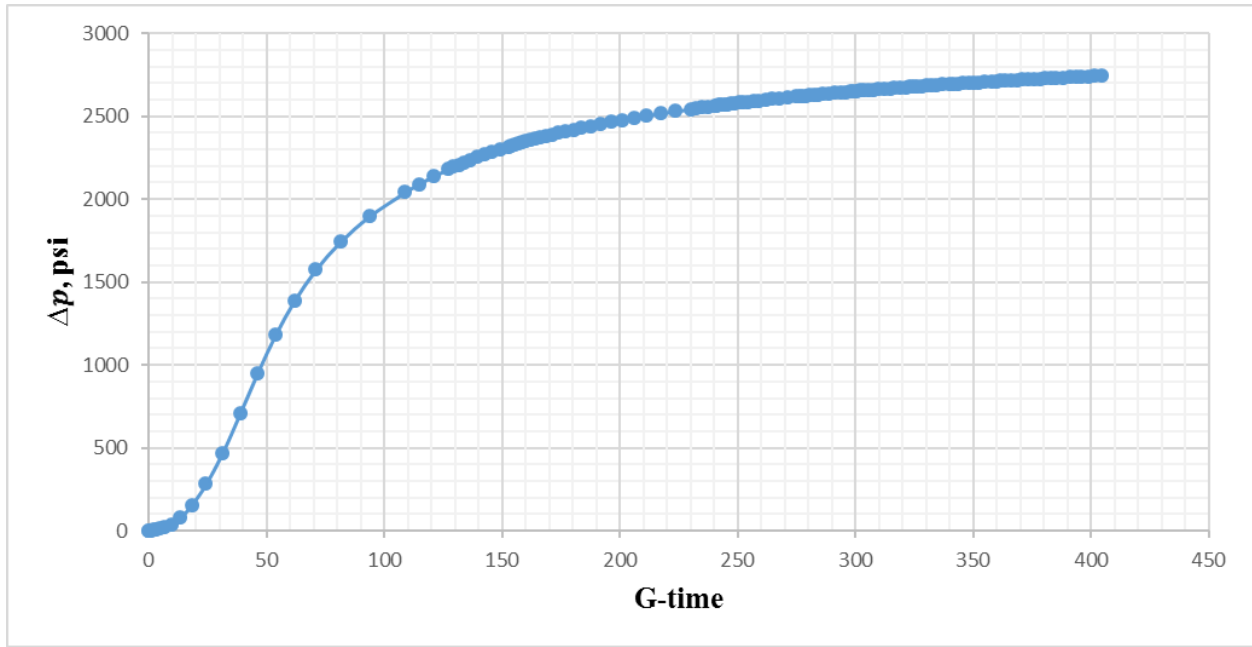


Figure 4.14 The plot of Δp versus G for Case 4

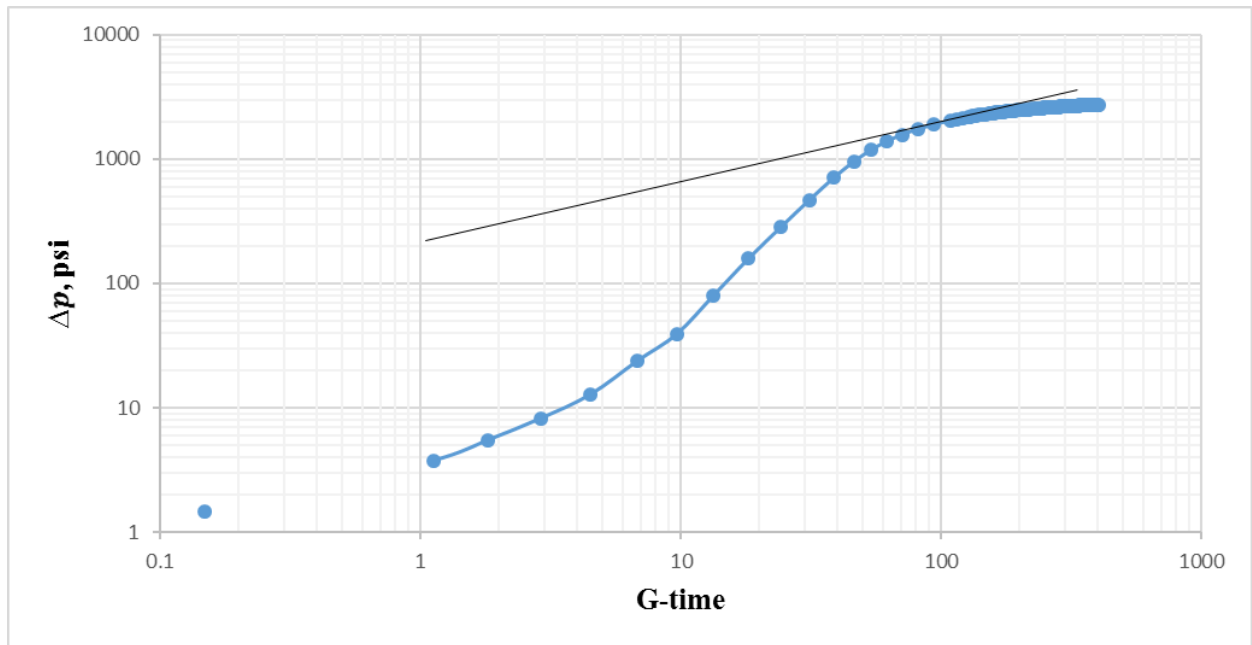


Figure 4.15 The log-log plot of Δp versus G for Case 4

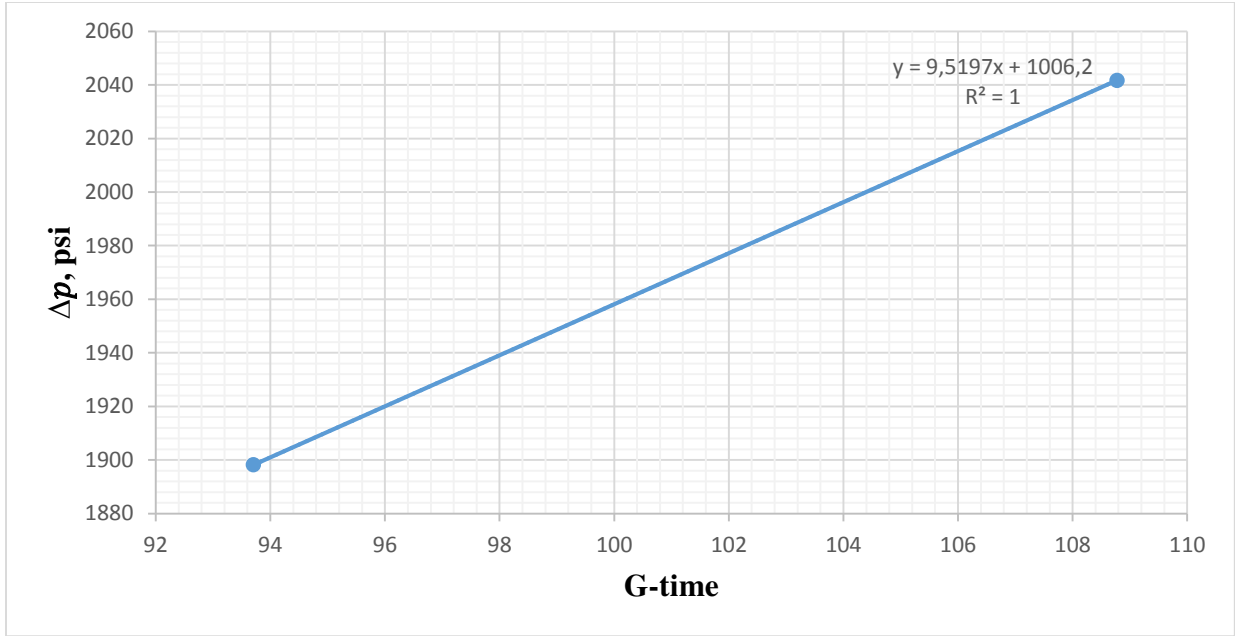


Figure 4.16 The plot of Δp versus G within the linear flow interval for Case 4

The leakoff coefficient is obtained from Equations 2.6 and 2.7 as follows:

$$C_L = \frac{2 \left[\frac{\pi(1-\nu^2)}{2E} \right] x_f m}{\pi \sqrt{t_p}} = \frac{2 \left[\frac{\pi(1-0.25^2)}{2 * 5.44 * 10^{-6}} \right] * 32.81 * 9.5197}{\pi * \sqrt{2}} = 38.0615 * 10^{-6} \text{ ft}/\sqrt{\text{min}}$$

Calculating the matrix permeability using the extended fracture half-length yields

$$k_m = \frac{1 * (38.0615 * 10^{-6})^2}{0.0000004127 * (0.00118 * (7410 - 5076))^2} = 0.00046 \text{ md}$$

On the other hand, the use of the fracture half-length at closure (15.2348 ft) leads to

$$k_m = \frac{1 * (177.225 * 10^{-6})^2}{0.0000004127 * (0.00118 * (7410 - 5076))^2} = 0.000128 \text{ md}$$

4.2 Discussions

First of all, for all cases considered in the simulated examples presented in this chapter, the G-function permeability estimates were much higher than the original matrix permeability. This can be attributed to the fact that the G-function permeability does not only represent the matrix permeability but also the contribution of fracture permeability. In other words, the G-function permeability is the composite response from both matrix and fracture permeability. Besides, as the matrix permeability increased, the error in the permeability estimates from G-function analysis increased. Moreover, the existence of a complex fracture network increased both the estimate and the error of the G-function permeability.

Second, the closure phenomenon took place much faster in the case of a higher permeability due to higher leakoff rate. More leakoff to the formation caused more complex fracture network, consisting of natural fractures and hydraulic fracture, which, in turn, resulted in faster closure than that in the case with only a hydraulic fracture. Besides, smaller residual aperture caused fractures to be closed sooner than the case with higher residual aperture because smaller residual fracture aperture caused more fluid for leakoff leading to faster fracture closure.

Additionally, closure pressures estimated from G-function analysis were always lower than the original minimum horizontal stress. The fluid staying in the fracture after closure was considered to be one of the reasons for having closure pressures less than the minimum horizontal stress. When the residual aperture became smaller, the estimated closure pressure was closer to the minimum horizontal stress. This also validated the theoretical assumption that the closure pressure would be equal to the minimum horizontal stress in case of a completely closing fracture.

Moreover, higher matrix permeability yielded higher leakoff rates. For a lower matrix permeability case, a higher leakoff rate was achieved with a more complex fracture network system. Having a smaller residual fracture aperture also generated higher leakoff rates than the cases with larger residual fracture aperture. Shorter fracture half-lengths at closure were generated in case of high leakoff rates.

Finally, analyzing the pressure fall-off data from a DFIT test which involved plotting of Δp versus G-time resulted in closer estimates of permeability using both extended fracture half-length and fracture half-length at closure. However, using fracture half-length at closure generated the best permeability estimates. This study also showed that the original Nolte analysis for DFIT analysis would yield better results for unconventional reservoirs whereas G-function analysis is better if it is used for higher permeability systems, such as conventional and tight gas reservoirs.

CHAPTER 5

CONCLUSIONS AND RECOMMENDATIONS

This study investigated the application of DFIT analysis in unconventional reservoirs and documented the sensitivity of results to the magnitude of permeability and existence of a complex fracture network as in a SRV. The DFIT data used in the study was generated through CFRAC (Complex Fracturing ReseArch Code), which is a hydraulic fracturing simulator developed by McClure and Horne (2013). There were four cases in which three essential parameters such as permeability, residual fracture aperture, and complex fracture network were studied in terms of their effects on G-function permeability, leakoff rate, closure pressure, and closure time.

The permeability estimations from G-function analysis were always higher than the original matrix permeability for the cases investigated in this work. When the matrix permeability was higher or there was a complex fracture network, the error in estimation of the G-function permeability was higher. Increasing matrix permeability and creating a more complex fracture network increased the leakoff rate. Additionally, having higher residual fracture aperture resulted in smaller leakoff rate. Higher leakoff rate decreased the fracture half-length at closure.

Closure pressures for all simulated cases were always lower than the minimum horizontal stress due to the existence of residual fracture aperture. Decreasing the residual fracture aperture caused closure pressure obtained from G-function analysis to be closer to the minimum horizontal stress. It was also observed that the fracture closure took place faster in the case of higher-permeability matrix and complex fracture network.

An important finding of this study was that analyzing the pressure fall-off data obtained from a DFIT test by plotting Δp versus G-time as originally proposed by Nolte yielded better

estimations of permeability. Moreover, use of the extended fracture half-length in calculations yielded nearly the original matrix permeability assigned in the simulations. Therefore, it was concluded that the original Nolte analysis for DFIT would produce better results for unconventional reservoirs whereas G-function analysis could be suitable for conventional and tight gas reservoirs where higher permeability and more homogeneous matrix are common occurrences.

In the future, simulations with more complex fracture networks having different natural fracture and hydraulic fracture features are recommended to further delineate the sensitivity of G-function analysis to fractured reservoir properties. Also, the effect of other parameters, such as porosity, total compressibility, and shear modulus on DFIT analysis should be investigated. Consideration of several field examples should also improve the confidence on the success of the original Nolte method in unconventional reservoirs.

REFERENCES

- Anderson, E., Bai Z., Bischof, C., Blackford, S., Croz, J. D., Demmel, J., Dongarra, J., Greenbaum, A., Hammarling, S., McKenney, A., and Sorensen, D. 1999. *LAPACK Users' Guide*, Third ed., Society for Industrial and Applied Mathematics, Philadelphia, PA.
- Amestoy, P. R., Davis, T. A., and Duff, I. S. 1996. An approximate minimum degree ordering algorithm. *SIAM Journal on Matrix Analysis and Applications*, 17 (4): 886-905. <https://doi.org/10.1137/S0895479894278952>.
- Amestoy, P. R., Davis, T. A., and Duff, I. S. 2004. Algorithm 837: AMD, an approximate minimum degree ordering algorithm. *ACM Transactions on Mathematical Software*, 30 (3): 381-388. <https://doi.org/10.1145/1024074.1024081>.
- Barree, R. D., Gilbert, J. V. and Miskimins, J. L. 2015. Diagnostic Fracture Injection Tests: Common Mistakes, Misfires, and Misdiagnoses. *SPE Production & Operations* 30 (2): 1-15. SPE-169539-PA. <https://doi.org/10.2118/169539-PA>.
- Barree, R. D, Barree, V. L and Craig, D. P. 2007. Holistic Fracture Diagnostics. Presented at the SPE Rocky Mountain Oil & Gas Technology Symposium, Denver, Colorado, 16-18 April. SPE-107877-MS. <https://doi.org/10.2118/107877-MS>.
- Barton, N., Bandis, S., and Bakhtar, K. 1985. Strength, deformation and conductivity coupling of rock joints. *International Journal of Rock Mechanics and Mining Sciences & Geomechanics Abstracts*. 22 (3): 121-140. [https://doi.org/10.1016/0148-9062\(85\)93227-9](https://doi.org/10.1016/0148-9062(85)93227-9).
- Bradley, A. M. 2014. Software for efficient static dislocation-traction calculations in fault simulators. *Seismological Research Letters*, 85 (6): 1358-1365. <https://doi.org/10.1785/0220140092>.
- Cinco-Ley, H. and Samaniego, V. F. 1981. Transient Pressure analysis for Fractured Wells. *Journal of Petroleum Technology* 33 (9): 1749-1766. SPE-7490-PA. <https://doi.org/10.2118/7490-PA>.

- Craig, D. P. and Jackson, R. A. 2017. Calculating the Volume of Reservoir Investigated During a Fracture-Injection/Falloff Test DFIT. Presented at the SPE Hydraulic Fracturing Technology Conference and Exhibition, The Woodlands, Texas, 24-26 January. SPE-184820-MS. <https://doi.org/10.2118/184820-MS>.
- Dongarra, J. J., Croz, J. D., Hammarling, S., and Hanson, R. J. 1988. An extended set of FORTRAN Basic Linear Algebra Subprograms. *ACM Transactions on Mathematical Software*, 14 (1): 1-17. <https://doi.org/10.1145/42288.42291>.
- Dongarra, J. J., Croz, J. D., Hammarling, S., and Hanson, R. J. 1988. Algorithm 656: an extended set of basic linear algebra subprograms: model implementation and test programs. *ACM Transactions on Mathematical Software*, 14 (1): 18-32. <https://doi.org/10.1145/42288.42292>.
- Dongarra, J. J., Croz, J. D., Hammarling, S., and Duff, I. S. 1990. A set of level 3 basic linear algebra subprograms. *ACM Transactions on Mathematical Software*. 16 (1): 1-17. <https://doi.org/10.1145/77626.79170>.
- Dongarra, J. J., Croz, J. D., Hammarling, S., and Duff, I. S. 1990. Algorithm 679: A set of level 3 basic linear algebra subprograms: model implementation and test programs. *ACM Transactions on Mathematical Software*, 16 (1): 18-28. <https://doi.org/10.1145/77626.77627>.
- Davis, T. A. 2006. *Direct Methods for Sparse Linear Systems*, SIAM, Philadelphia, PA.
- Davis, T. A. 2004. A column pre-ordering strategy for the unsymmetric-pattern multifrontal method. *ACM Transactions on Mathematical Software*, 30 (2): 165-195. <https://doi.org/10.1145/992200.992205>.
- Davis, T. A. 2004. Algorithm 832: UMFPACK, an unsymmetric-pattern multifrontal method. *ACM Transactions on Mathematical Software*, 30 (2): 196-199. <https://doi.org/10.1145/992200.992206>.
- Davis, T. A., and Duff, I. S. 1997. An unsymmetric-pattern multifrontal method for sparse LU factorization. *SIAM Journal on Matrix Analysis and Applications*, 18 (1): 140-158. <https://doi.org/10.1137/S0895479894246905>.

- Davis, T. A., and Duff, I. S. 1999. A combined unifrontal/multifrontal method for unsymmetric sparse matrices. *ACM Transactions on Mathematical Software*, 25 (1): 1-19. <https://doi.org/10.1145/305658.287640>.
- Economides, M.J., and Nolte, K.G. 1987. *Reservoir Stimulation*, John Wiley and Sons, New York.
- Eker, I., Kazemi, H., Kurtoglu, B., and Torcuk, M. A. 2015. Performance Analysis of Unconventional Shale Reservoirs. In *Fundamentals of Gas Shale Reservoirs*, Wiley, 283-300. <https://doi.org/10.1002/9781119039228.ch13>.
- Guennebaud, G., and Jacob, B. 2010. Eigen v3. <http://eigen.tuxfamily.org> (Accessed 30 February 2018).
- Halliburton Testing and Subsea. 2012. DFIT™ Test Analysis When On Vacuum At The Surface, http://www.halliburton.com/public/ts/contents/Papers_and_Articles/web/DFIT-Analysis-When-On-Vacuum-At-The-Surface.pdf (Accessed 30 March 2017).
- Jung, H. 2015. *Numerical Modeling for Identification of Closure Pressure from Diagnostic Fracture Injection Tests*. MS Thesis, The University of Texas at Austin, Austin, Texas.
- Lawson, C. L., Hanson, R. J., Kincaid, D., and Krogh, F. T. 1979. Basic Linear Algebra Subprograms for FORTRAN usage. *ACM Transactions on Mathematical Software*, 5 (3): 308-323. <https://doi.org/10.1145/355841.355847>.
- McClure, M. W., Babazadeh, M., Shiozawa, S., and Huang, J. 2015. Fully coupled hydromechanical simulation of hydraulic fracturing in three-dimensional discrete fracture networks. Presented at the SPE Hydraulic Fracturing Technology Conference, The Woodlands, Texas, 3-5 February. SPE-173354-MS. <https://doi.org/10.2118/173354-MS>.
- McClure, M. W., and Horne, R. N. 2013. *Discrete Fracture Network Modeling of Hydraulic Stimulation: Coupling Flow and Geomechanics*, Springer. <https://doi.org/10.1007/978-3-319-00383-2>.

- McClure, M. W. 2012. *Modeling and characterization of hydraulic stimulation and induced seismicity in geothermal and shale gas reservoirs*. PhD Thesis, Stanford University, Stanford, California.
- Nolte, K. G. 1979. Determination of Fracture Properties from Fracturing Pressure Decline. Presented at the 54th SPE Annual Technical Conference and Exhibition, Las Vegas, Nevada, 23-26 September. SPE-8341-MS. <https://doi.org/10.2118/8341-MS>.
- Nolte, K. G. 1986. A General Analysis of Fracturing Pressure Decline With Application to Three Models. *SPE Formation Evaluation* 1 (6): 571-583. SPE-12941-PA. <https://doi.org/10.2118/12941-PA>.
- Nolte, K. G. 1988. Principles of Fracture Design Based on Pressure Analysis. *SPE Production Engineering*, 3 (1): 22-30. SPE-10911-PA. <https://doi.org/10.2118/10911-PA>.
- Norbeck, J., and Horne, R. 2015. Injection-triggered seismicity: an investigation of porothermoelastic effects using a rate-and-state earthquake model. Presented at the Fourtieth Workshop on Geothermal Reservoir Engineering, Stanford University, Stanford, California, 26-28 January.
- Olson, J. E. 2007. *Fracture aperture, length and pattern geometry development under biaxial loading: a numerical study with applications to natural, cross-jointed systems*. Geological Society, London, Special Publications, 289 (1): 123-142. <https://doi.org/10.1144/SP289.8>.
- Olson, J., and Sheibani, F. 2013. Stress Intensity Factor Determination for Three-Dimensional Crack Using the Displacement Discontinuity Method with Applications to Hydraulic Fracture Height Growth and Non-Planar Propagation Paths. Presented at the ISRM International Conference for Effective and Sustainable Hydraulic Fracturing, Brisbane, Australia.
- Sneddon, I. N. 1946. The distribution of stress in the neighborhood of a crack in an elastic solid. *Proceedings of the Royal Society of London Series A* 187 (1009): 229-260. <https://doi.org/10.1098/rspa.1946.0077>.
- Vinsome, P. K. W., and Westerveld, J. 1980. A Simple Method For Predicting Cap And Base Rock Heat Losses In Thermal Reservoir Simulators. *Journal of Canadian Petroleum Technology*, 19 (3): 1-5. PETSOC-80-03-04. <https://doi.org/10.2118/80-03-04>.

Willis-Richards, J., Watanabe, K., and Takahashi, H. 1996. Progress toward a stochastic rock mechanics model of engineered geothermal systems. *Journal of Geophysical Research*, 101 (B8): 17481-17496. <https://doi.org/10.1029/96JB00882>.